Atypical Protein Kinase C Promotes its own Asymmetric Localisation by Phosphorylating Cdc42 in Polarising Cells

John Packer[1,5], Alicia G. Gubieda[1,5], Aaron Brooks[1,6], Lars N. Deutz[2,6], Iolo Squires[1,6], Shona Ellison[3], Sundar Ram Naganathan[4], Adam J.M. Wollman[1], Daniel J. Dickinson[2], Josana Rodriguez[1,7,*]

[1] Newcastle University Biosciences Institute, Newcastle University, Newcastle upon Tyne, NE2 4HH, UK

[2] Department of Molecular Biosciences, University of Texas at Austin, Austin, Texas, USA

[3] The Francis Crick Institute, London, NW1 1AT, UK

[4] Department of Biological Sciences,
Tata Institute of Fundamental Research,
Mumbai 400005, India

[5]These authors contributed equally
[6]These authors contributed equally
[7]Lead contact

*Correspondence: josana.rodriguez@ncl.ac.uk

SUMMARY

Atypical protein kinase C (aPKC) is a major regulator of cell polarity. Acting in conjunction with Par6, Par3 and the small GTPase Cdc42, aPKC becomes asymmetrically localised and drives the polarisation of cells. aPKC activity is crucial for its own asymmetric localisation, suggesting a hitherto unknown feedback mechanism contributing to polarisation. Here we show in *C. elegans* zygotes that the feedback relies on CDC-42 phosphorylation at serine 71 by aPKC, which in turn results in aPKC dissociation from CDC-42. The dissociated aPKC then associates with PAR-3 clusters, which are transported anteriorly by actomyosin-based cortical flow. Moreover, the turnover of aPKC-mediated CDC-42 phosphorylation regulates the organisation of the actomyosin cortex that drives aPKC asymmetry. Given the widespread role of aPKC and Cdc42 in cell polarity, this form of self-regulation of aPKC may be vital for the robust polarisation of many cell types.

Keywords: asymmetric cell division, cell polarity, cell patterning, embryo axis, PAR proteins, atypical protein kinase C, aPKC, membrane protein complex dynamics, aPKC self-regulatory feedback, actomyosin cortex dynamics, phosphoregulation of CDC-42

Key findings/graphical abstract:

- aPKC-mediated phosphorylation of CDC-42 on serine 71 dissociates aPKC from CDC-42
- Dissociation of aPKC from CDC-42 promotes the anterior membrane localisation of aPKC with PAR-3
- CDC-42 phosphorylation prevents the anterior membrane enrichment of CDC-42
- Phosphorylated CDC-42 is enriched at actomyosin foci and induces their disorganisation

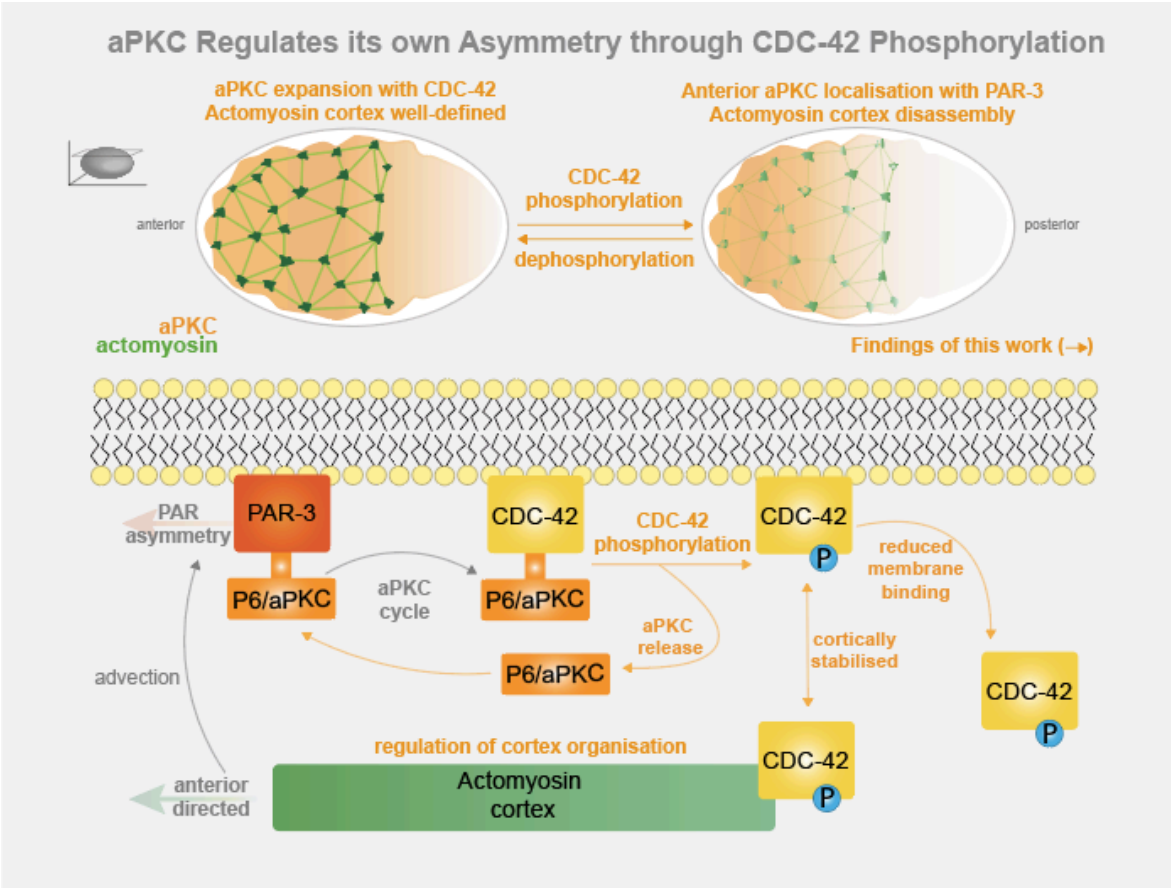

INTRODUCTION

The polarisation of cells, or asymmetric distribution of cellular components and functions, is key to the generation of cellular diversity. Cell polarity depends on the asymmetric localisation of molecules within the cell.[1–3] Prominent examples are the PAR proteins, conserved effectors of cell polarity, initially identified in *Caenorhabditis elegans.*[4–6] The PDZ domain proteins Par3 and Par6, the small guanosine triphosphatase (GTPase) Cdc42 and atypical protein kinase C (aPKC) frequently work together to polarise cells. For example, they specify the apical domain in epithelial cells,[7,8] the front in migrating cells[9,10] and the domain of an asymmetrically dividing cell that will be inherited by one of the daughter cells.[11,12]

aPKC is an essential component of this polarising network,[13] its asymmetric membrane localisation and activity being controlled by the other network members. Par6 is considered an aPKC co-factor that brings aPKC to the membrane through its interaction with Par3 or Cdc42.[14–26] Other mechanisms of membrane localisation have also been reported, where aPKC can be directly recruited to the membrane through its interaction with Par3[27,28] and possibly even on its own through a newly identified polybasic domain in aPKC sequence that is capable of targeting PAR-6/aPKC to the plasma membrane.[29,30] How these various mechanisms of membrane association are regulated, influence each other, and impact overall aPKC asymmetry remain unclear. aPKC activity is regulated by both Par6 and Par3, which have been described to enhance or suppress aPKC depending on the system studied.[14,15,18,31–38] In contrast, there is more consensus for Cdc42 supporting that, in its active GTP-bound state, Cdc42 can recruit PAR-6/aPKC to the membrane and promote aPKC kinase activity.[14,19,36,37,39]

PAR protein interactions and their membrane localisation are spatiotemporally regulated in polarising cells to define the aPKC membrane domain. For example, the cell cycle kinases Aurora A and Polo reduce the membrane association of this PAR network, coordinating cell polarisation with the cell cycle.[34,40–42] Moreover, mutual antagonism is a prevailing mechanism to create opposing membrane domains of PARs. The kinase Par1 phosphorylates Par3, preventing Par3 oligomerisation and Par3 interaction with aPKC, in this way restricting aPKC from accumulating in the Par1 domain.[43] Conversely, aPKC phosphorylates Par1, preventing Par1 build-up in the aPKC domain.[44–47] Recently, growing evidence indicates that aPKC activity, in addition to excluding proteins from opposing domains, also restricts itself to its own domain.[36,48] However, the mechanism by which aPKC controls its own distribution is unknown. Here, we have investigated this problem during polarisation of the *C. elegans* zygote.

The *C. elegans* zygote becomes polarised along the antero-posterior axis in an aPKC dependent manner.[6] This polarisation drives the zygote's asymmetric division, leading to anterior somatic and posterior germline precursors. Polarisation starts after fertilisation, when the network of aPKC, Par6, Par3 and Cdc42 (PKC-3, PAR-6, PAR-3 and CDC-42 in *C. elegans*, known as anterior PARs, aPARs) become asymmetrically localised to the anterior membrane of the zygote in response to the anterior-directed movement of the actomyosin cortex.[49,50] This movement is known as the actomyosin cortical flow and depends primarily on the small GTPase RhoA (RHO-1 in *C. elegans*) signalling.[51–55] In the *C. elegans* zygote, the membrane localisation of PAR-6/aPKC depends on PAR-3 or CDC-

42.[6,22,36,56,57] PAR-6/aPKC segregate most efficiently when in membrane clusters, which depend on PAR-3 oligomerisation and are mechanically coupled to actomyosin cortical flow.[36,40,58–63] Moreover, opposing posterior PARs; the kinase PAR-1, the scaffolding protein PAR-2, LGL-1 and the CDC-42 GAP, CHIN-1, also promote the segregation of aPARs to the anterior.[46,64–69] Previously, we showed that aPKC kinase activity is also needed to restrict the size of the aPAR domain because, when aPKC is inactive, aPKC and PAR-6 remain localised throughout the zygote's membrane even though PAR-3 still becomes anteriorly localised.[36] Similar observations have been reported in the *Drosophila* neuroblast, where inactivation of aPKC leads to its basal expansion.[48] In the *C. elegans* zygote, we found this aPKC domain expansion to be dependent on CDC-42.[36] How aPKC mediates its own asymmetry, the identity of the phosphorylation targets, and the mechanisms involved, however remain unknown.

Our previous work suggested that aPKC kinase activity could be regulating its interactions with the other members of the aPAR network.[36] Given that inactive aPKC remains bound to CDC-42 occupying the entire zygote's membrane, we questioned if CDC-42 could be a substrate of aPKC and whether CDC-42 phosphorylation could mediate aPKC dissociation from CDC-42. Here, we report that aPKC activity promotes the phosphorylation of CDC-42 on serine 71. This phosphorylation regulates aPARs in two ways: it reduces the membrane localisation of CDC-42 and destabilises aPKC interaction with CDC-42 at the membrane. Once released from CDC-42, aPKC is free to be recruited into PAR-3 clusters on the membrane, promoting aPKC segregation and the polarisation of the zygote. Furthermore, we find that turnover between non-phosphorylated and phosphorylated CDC-42 on serine 71 is necessary for the correct organisation of the actomyosin cortex during polarity establishment and maintenance. Our results reveal how aPKC activity can define its own domain of action by controlling the dynamic protein interactions of aPARs and contributing to the organisation of the actomyosin cortex, both through phosphorylation of CDC-42.

RESULTS

aPKC-dependent phosphorylation of CDC-42 reduces CDC-42 membrane localisation.

To test our hypothesis that aPKC controls its own asymmetric localisation through phosphorylation of CDC-42, we first performed an *in vitro* kinase assay using purified recombinant human aPKC and Cdc42, which showed that aPKC phosphorylates Cdc42 (**Fig. 1A**). We identified three predicted aPKC phosphorylation sites in CDC-42 using the group-based prediction tool GPS 5.0[70]: T3, S71 and S106. Among these, S71 is evolutionary conserved from worms to humans (**Fig. 1B**) and has been reported to regulate Cdc42 function in mammalian tissue culture cells, impacting Cdc42 interaction with downstream effectors.[71–73] To investigate if S71 could be an aPKC phosphosite, we compared phosphorylation levels of recombinant MBP-tagged CDC-42 vs. MBP-tagged non-phosphorylatable CDC-42 variant (serine 71 to alanine, S71A) in an *in vitro* kinase assay. Here we used human aPKC co-purified with Par6, which supports aPKC interaction with Cdc42, and confirmed that aPKC can phosphorylate wild-type CDC-42 *in vitro* (**Fig.1A and 1C**). Phosphorylation of CDC-42 strongly decreased when we mutated serine 71 to alanine (S71A) (**Fig. 1C**), suggesting that this is the primary site on which aPKC phosphorylates CDC-42. We also detected the previously described aPKC phosphorylation of Par6 (**Fig. 1C**).[74] Phosphorylation of Par6 did not occur in the absence of CDC-42 (**Fig. 1C**, middle lane), supporting the known role of CDC-42 in promoting aPKC kinase activity.[14,19,36,37,39] Interestingly, phosphorylation of Par6 was also reduced in the presence of CDC-42 (S71A) compared to that observed in the presence of wild-type CDC-42 (**Fig. 1C**). Thus, the S71A point mutation could affect the ability of CDC-42 to activate aPKC, or alternatively, if aPKC is not capable of phosphorylating CDC-42(S71A), this could lead to an aPKC/CDC-42 stalled complex, blocking aPKC activity towards other sites. Together, these results show that aPKC can phosphorylate CDC-42 *in vitro* and that a S71A mutation prevents CDC-42 phosphorylation by aPKC. These outcomes prompted us to determine *in vivo* if this putative aPKC phosphosite can regulate CDC-42 localisation and CDC-42 association with PAR-6/aPKC, and whether these factors impact the asymmetric localisation of aPKC.

Characterisation of the cellular localisation of transgenically expressed GFP::CDC-42(S71A) (non-phosphorylatable) and GFP::CDC-42(S71E) (phosphomimetic) showed that CDC-42 phosphorylation on S71 controls the membrane localisation and asymmetry of CDC-42. We observed wild-type CDC-42 localised to the membrane of the zygote, showing an anterior enrichment once polarity is established (maintenance stage) (**Fig.1D**), with higher levels of CDC-42 at the anterior membrane versus the posterior (**Fig.1E**). This led to a slight enrichment of CDC-42 at the anterior daughter cell after cell division (**Fig. 1D**). The non-phosphorylatable (S71A) variant presented an asymmetry in the zygote similar to that observed for wild-type CDC-42 (**Fig.1D**), showing a small increase in its anterior membrane localisation compared to that present in CDC-42 (**Fig.1E & F**). On the other hand, the phosphomimetic mutant's membrane localisation was severely disrupted, not presenting an anterior enrichment, and its membrane levels were very weak throughout the zygote's AP axis, only matching those of CDC-42 and CDC-42(S71A) at the posterior membrane (**Fig. 1D-F**). Note that CDC-42(S71E) also causes strong embryonic lethality compared to control and CDC-42(S71A) (**Fig. S1A**). The weak cortical localisation observed for CDC-42(S71E) is not due to low expression levels, given that we observed similar CDC-42 protein levels in CDC-42(S71E) mutant compared to those present in wild-type CDC-42 and CDC-42(S71A)

variant (**Fig. S1B**). Therefore, we conclude that the membrane binding of CDC-42(S71E) variant is reduced.

We hypothesised that this reduction in CDC-42 membrane localisation and asymmetry could be a result of CDC-42 phosphorylation disrupting CDC-42 interaction with aPARs. To test this, we depleted PAR-6 and analysed CDC-42 localisation (**Fig. S2**). PAR-6 depletion in the CDC-42 wild-type strain led to loss of CDC-42 membrane localisation just like that observed for the CDC-42(S71E) variant (**Fig. S2 D-F**), suggesting that PAR-6 plays an important role in the membrane localisation of CDC-42. PAR-6 depletion in the CDC-42(S71A) mutant led to loss of CDC-42 asymmetry but some CDC-42 remained at the membrane (**Fig. S2 E**). This could suggest that phosphorylation of CDC-42 on S71 can also destabilise CDC-42 membrane localisation independently of PAR-6. Alternatively, in the CDC-42(S71A) variant the interaction between PAR-6 and CDC-42 could be stabilised compared to that present in CDC-42 wild type embryos and hence any residual PAR-6 after depletion could be sufficient to partially rescue the membrane localisation of CDC-42. Overall, these results indicate that PAR-6 is necessary for CDC-42 localisation to and asymmetry at the membrane, and that phosphorylation of CDC-42 disrupts this role of PAR-6.

Tracking the movement of individual molecules of CDC-42 in the plane of the membrane using near-TIRF microscopy (HILO[75]), we found that, in the zygote, CDC-42 diffuses more quickly than aPARs (**Fig. 1 G-I**).[58,63,76–78] Because of the slower dynamics of PAR-6 at the membrane compared to CDC-42 (**Fig. 1 G-I**), we reasoned that if CDC-42 phosphorylation were to reduce PAR-6-dependent control of CDC-42 localisation, then this phosphorylation should lead to an increase in the membrane dynamics of CDC-42 molecules. We therefore analysed the nanoscale dynamics of the different CDC-42 variants at the membrane. In all variants the distribution of CDC-42 diffusion coefficients (D) appeared bimodal (**Fig. S3A-C)** and were well fit (R^2>0.95) by a model comprising two mobility states: mobile (D> 0.1 μm^2/s) and immobile (D< 0.1 μm^2/s). We further confirmed these two states in our CDC-42 diffusion data by using nonparametric Bayesian statistics (SMAUG[79]) **(Fig. S3E).** Studying the immobile and mobile states in the different CDC-42 variants we observed that the mobile fraction of CDC-42(S71E) diffused significantly faster compared to the mobile fractions of wild-type CDC-42 or CDC-42(S71A) **(Fig. 1H)**. Moreover, the proportion of immobile CDC-42(S71E) was reduced to levels close to the minimum possible levels based on simulations, i.e. CDC-42(S71E) presented near total reduction in immobile CDC-42 (**Fig. 1I** and **Fig. S3F)**. Note that we detected similar number of CDC-42 molecules across strains, indicating that the overall recruitment of CDC-42(S71E) to the membrane is not reduced rather its stability at the membrane might be impaired as suggested by its altered mobility (**Fig. 1H** see legend). We also tracked PAR-6 dynamics under the same imaging conditions (**Fig. 1H, I** and **Fig. S3D**), highlighting that CDC-42 wild type and CDC-42(S71A) presented dynamics closer to those of PAR-6 than CDC-42(S71E) did. The phosphomimetic mutant's faster dynamics would agree with a reduced interaction of this CDC-42 variant with the slower population of PAR-6. In summary, our CDC-42 phosphomutant analyses indicate that phosphorylation of CDC-42 leads to destabilisation of CDC-42 at the membrane and to loss of CDC-42 asymmetry, possibly through disruption of CDC-42/aPAR interaction.

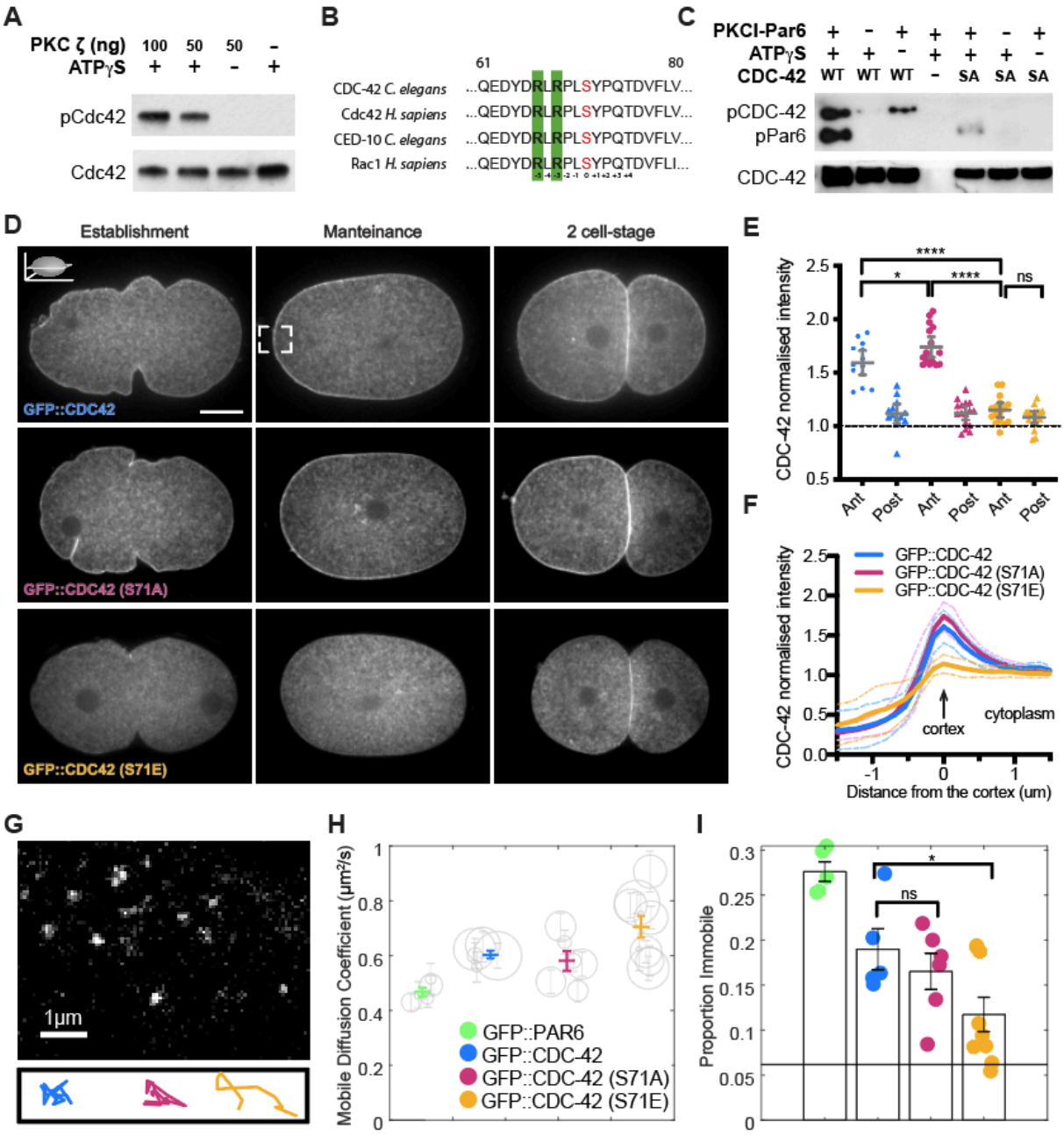

Figure 1. Analysis of CDC-42 phophomutants indicates that phosphorylation of serine 71 reduces CDC-42 asymmetry and membrane localisation. A. aPKC phosphorylates CDC-42 *in vitro*. Immunoblot showing that human Cdc42 can be phosphorylated by human aPKC (PKC ζ) *in vitro* using purified recombinant proteins incubated with ATP-gamma-S. After each kinase reaction, the products were alkylated, and thiophosphorylated Cdc42 (pCdc42) was detected with an anti-thiophosphate ester antibody (see methods). Total Cdc42 detection is shown as loading control. **B.** Protein sequence conservation for Cdc42 and Rac1 (CED-10, *C. elegans* homologue) around serine 71 (red). Conserved arginines, which are part of aPKC consensus site are highlighted (green). **C.** Immunoblot showing the detection of phosphorylated CDC-42 and Par6 (positive control) from an *in vitro* kinase assay containing co-purified human PKCI - Par6 and wild-type *C. elegans* CDC-42 (WT) or CDC-42(S71A) (SA). Thiophosphorylation detection was done as in (A). In three independent blots we consistently observed more phosphorylation of CDC-42 wild type compared to CDC-42(S71A) (~17 times more, after loading correction and background subtraction, i.e. subtraction of signal detected in the corresponding minus ATPγS lane). A similar increase in phosphorylation was observed for Par6 in the CDC-42 kinase reaction compared to that of CDC-42(S71A). **D.** Representative midsection confocal images of live embryos at establishment, maintenance and 2-cell stage showing GFP::CDC-42, GFP::CDC-42(S71A) and GFP::CDC-42(S71E). Zygotes are always oriented anterior to the left. In these CDC-42 reporter lines we deplete endogenous CDC-42 by RNAi that targets its 3' UTR, in this way preventing possible phenotypic rescue by endogenous CDC-42. **E.** CDC-42 anterior and posterior cortical intensities (values are normalised by its corresponding cytoplasmic CDC-42 levels) observed in CDC-42, CDC-42(S71A) and CDC-42(S71E) maintenance stage embryos (graph shows all data points and mean ± CI 95%). Note that CDC-42(S71E) presents a very weak cortical localisation with no asymmetry (no difference in intensity at anterior vs. posterior). **F.** CDC-42 intensity profiles spanning the anterior membrane of CDC-42, CDC-42(S71A) and CDC-42(S71E) maintenance stage zygotes, showing mean ± SD. Briefly, a 60x60 pixel area from a straightened anterior cortex (see inset in A in GFP::CDC-42 maintenance) was projected in the y-axis to give a cross section profile spanning the cortex/membrane. The values are normalised so that the cytoplasmic levels are set to 1. Number of embryos studied in D. and E.: 13 CDC-42, 16 CDC-42(S71A), and 16 CDC-42(S71E). **G.** A representative HILO image of wild-type CDC-42 at the membrane. Below we show representative tracks obtained by following CDC-42 particles at the membrane in the different CDC-42 variants. **H.** Graph showing the diffusion coefficients (D) of the mobile fraction of CDC-42 variants and PAR-6, obtained from gamma fits to all mobile tracked data (coloured lines, errors represent 95% confidence intervals on the fits). See Fig. S3. Diffusion coefficients of gamma fits for mobile data obtained from individual embryos is shown by the position of the grey circles (circle size represents the number of tracks analysed per embryo and the lines represent 95% confidence intervals on the fits). **I.** Proportion of tracks found in the immobile fraction ($D < 0.1\ \mu m^2/s$) in each condition (graph shows all data points and mean ± SEM). Horizontal black line indicates the limit of detection of immobile fraction (baseline, See Fig. S3F). Average number of tracks (± SEM) at maintenance stage for the embryos analysed in E and F, CDC-42: 3295 ± 57 tracks/embryo in 5 embryos; CDC-42(S71A): 3047 ± 62 in 6 embryos; CDC-42(S71E): 3532 ± 47 in 9 embryos and PAR-6: 1380 ± 790 in 4 embryos. Unpaired, two-tail Student's t-test *p<0.05, ****p<0.0001, ns not significant. Scale bar in establishment zygote: 10 µm. See also Fig. S1A-B, S2 and S3.

Phosphorylation of CDC-42 at serine 71 promotes the dissociation of aPKC from CDC-42 and restricts aPKC to the anterior membrane

We sought to directly test if phosphorylation of S71 affected the interaction between CDC-42 and PAR-6/aPKC. Although PAR-6/aPKC can bind to GTP-locked mutants of CDC-42, both *in vitro* and in co-immunoprecipitation experiments, recent evidence suggests that native CDC-42/PAR-6 complexes are found at the plasma membrane and are disrupted by cell lysis in detergent.[80] Therefore, we tested CDC-42 association with aPKC using two independent approaches that aimed to preserve the membrane as intact as possible. First, we artificially recruited wild-type CDC-42, CDC-42(S71A) or CDC-42(S71E) to the membrane of polarised zygotes and measured their ability to recruit aPKC. The enhanced cortical localisation of these GFP::CDC-42 constructs was achieved through a membrane tethered nanobody that recognises GFP (PH-GBP[36])and recruits these constructs to the membrane of the zygotes at similar levels (**Fig. S1. C & D**). As expected, under this experimental set up (**Fig. 2A**), we observed that the enhanced membrane localisation of CDC-42 via PH-GBP increased PKC-3 membrane levels, compared to those observed in the absence of the PH-GBP construct (**Fig. 2C & D**, mostly observed for CDC-42(S71A) variant). Note that PKC-3 is still mostly recruited at the anterior, although CDC-42 is observed throughout the membrane (**Fig. S1. C & D**), indicating that a factor at the posterior of the zygote reduces the cortical recruitment of aPKC by CDC-42 and/or a factor at anterior promotes it, likely candidates would be the CDC-42 GEF, CHIN-1, at posterior and PAR-3 at anterior. Upon enhanced membrane recruitment of the different CDC-42 phosphomutants, we observed that anterior aPKC levels at the membrane were greater in the non-phosphorylatable form compared to wild-type CDC-42, whilst the phophomimetic mutant displayed reduced aPKC membrane levels (**Fig. 2C and D**). A similar trend was observed in the phosphomutants without PH-GBP, likely reflecting association of GFP::CDC-42 variants with the plasma membrane via normal cellular activation mechanisms. These results support that phosphorylation of CDC-42 on S71 can lead to the disruption of CDC-42/PAR-6/aPKC complex.

Next, we directly measured the interaction between CDC-42 and aPKC using single-cell, single-molecule pull-down experiments (sc-SiMPull[26,80]). We used a pulsed infrared laser to instantaneously lyse single zygotes in the presence of an amphipathic polymer that forms lipid nanodiscs from the native cellular membrane. Then, we captured GFP::CDC-42 molecules using anti-GFP nanobodies immobilized on a glass coverslip, identified those associated with labelled HaloTag::aPKC, and measured the dissociation rate constant (k_{off}) of the CDC-42/aPKC complex (**Fig. 2E**). We readily detected complexes containing GFP::CDC-42 variants and endogenous Halo::aPKC when we lysed zygotes in the presence of diisobutylene maleic acid (DIBMA) to form lipid nanodiscs. We observed that mutations of S71 altered the stability of these complexes: the S71E variant exhibited a k_{off} of 0.100 ± 0.012 s^{-1}, which was approximately 2-fold faster than the S71A variant (k_{off} = 0.060 ± 0.004 s^{-1}) or wild-type GFP::CDC-42 (k_{off} = 0.059 ± 0.008 s^{-1}) (**Fig. 2F and S4**). These data demonstrate that aPKC interacts more stably with CDC-42(S71A) than with CDC-42(S71E), further suggesting that phosphorylation destabilizes CDC-42/aPKC association.

We recently reported that CDC-42/PAR-6 complexes are more stable during polarity maintenance, when *cdc-42* is strongly required for normal PAR-6/aPKC localisation.[80] Remarkably, the CDC-42/aPKC k_{off} values that we measured for the S71A and S71E

variants were very similar to the wild-type CDC-42/PAR-6 k_{off} values during maintenance and establishment, respectively (**Fig. 2F**). Note that the PAR-6 and aPKC dissociate from each other approximately 50-fold slower than either protein dissociates from CDC-42;[26] thus, the k_{off} values that we are comparing here most likely reflect dissociation of PAR-6/aPKC heterodimers from CDC-42. These results suggest that phosphorylation of CDC-42 by aPKC may account for the differential stability of CDC-42/PAR-6/aPKC complexes during polarity establishment compared to polarity maintenance.

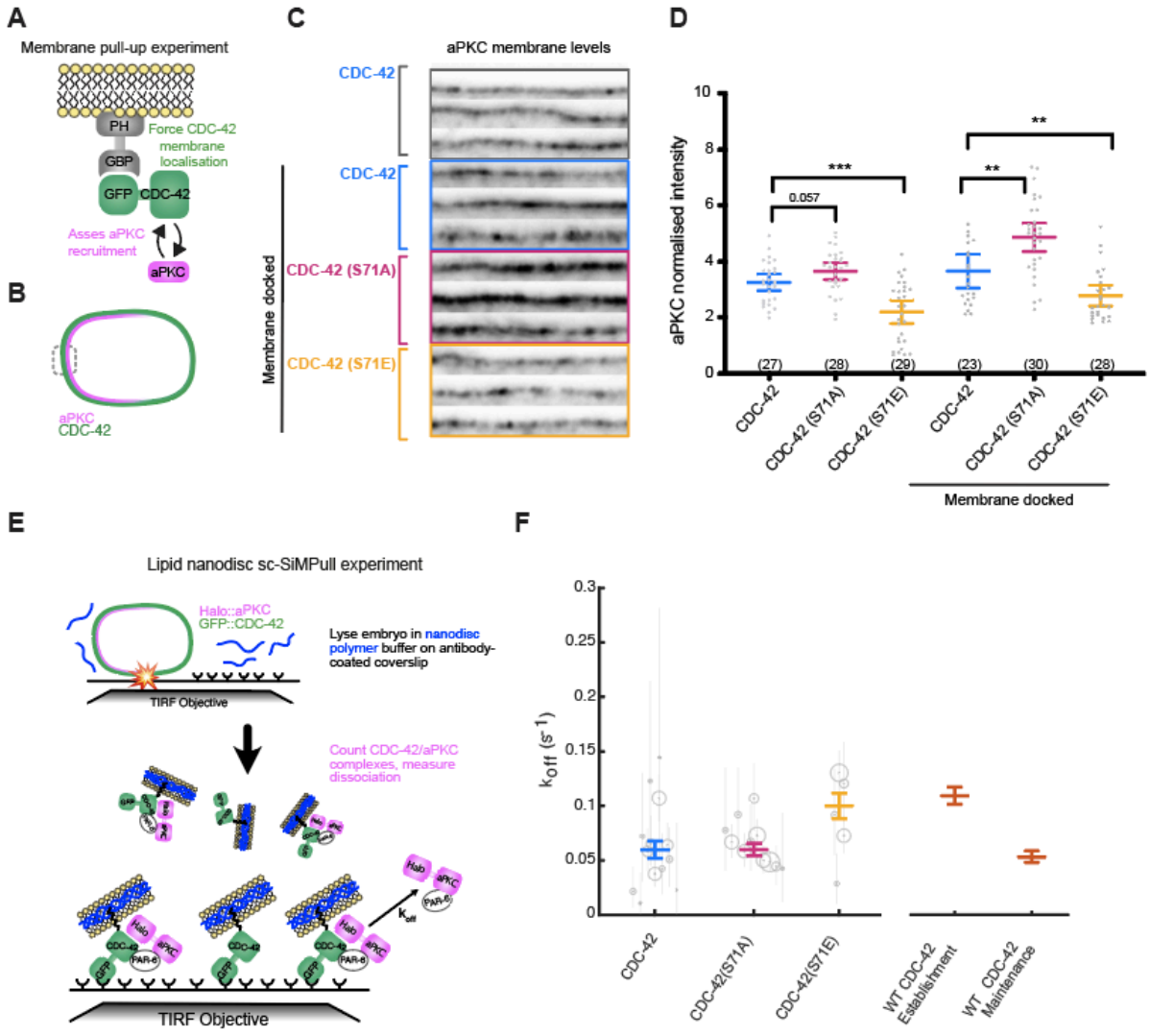

Figure 2. CDC-42 phosphorylation on serine 71 prevents CDC-42-dependent cortical recruitment of aPKC and promotes CDC-42/aPKC dissociation. A. Graphical representation of the experimental set up. Briefly, we use a membrane-tethered nanobody against GFP (PH-GBP) that can dock at the membrane GFP::CDC-42, GFP::CDC-42(S71A) or GFP::CDC-42(S71E). **B.** Zygotes with membrane-docked CDC-42 are immunostained for aPKC to determine aPKC membrane levels at the anterior domain (anterior-most selected region). **C.** Representative anterior membrane regions (three per condition) showing aPKC levels in the non-membrane docked GFP:CDC-42 reporter and in the membrane-docked GFP::CDC-42, GFP::CDC-42(S71A) and GFP::CDC-42(S71E) reporters (in all CDC-42 reporters endogenous CDC-42 is depleted). **D.** Average aPKC intensity values at the anterior membrane (measured in a 60x60 pixel area from a straightened anterior-most cortex) of zygotes during polarity maintenance. Anterior membrane intensity of aPKC for each zygote is normalised with its corresponding aPKC cytoplasmic level (graph shows all data points and mean ± CI 95%). Significant differences in the levels of anterior aPKC are observed for membrane docked GFP::CDC-42(S71A) and GFP::CDC-42(S71E) when compared to membrane-docked wild-type CDC-42. Number of embryos analysed in each condition are indicated in the graph. Unpaired, two-tail Student's t-test **p<0.01, ***<0.001. See also Figure S1C-E. **E.** Graphical representation of the lipid nanodisc single-cell pull-down (sc-SiMPull) experiment. Cells expressing GFP::CDC-42 variants and carrying endogenously tagged HaloTag::aPKC are lysed using a pulsed infrared laser in the presence of amphipathic polymers to form native lipid nanodiscs. sc-SiMPull was used to capture GFP::CDC-42 variants, which were detected using single-molecule TIRF microscopy. Complexes containing HaloTag::aPKC were identified and dissociation rate constants (k_{off}) of those complexes were measured (see Methods and Fig. S4). **F.** Dissociation rate constants measured for CDC-42/aPKC, CDC-42(S71A)/aPKC and CDC-42(S71E)/aPKC complexes extracted from late establishment and maintenance stage zygotes. Gray circles represent individual experiments, with the size of the circle indicating the number of CDC-42/aPKC complexes captured from each zygote and the error bars representing the Bayesian 95% credible interval for the estimated k_{off}. Colored bars show the maximum probability estimate and Bayesian 95% credible intervals for the k_{off} obtained by pooling all single-molecule measurements. n = 897 total CDC-42/aPKC complexes from 13 embryos (WT); n = 1,635 total CDC-42/aPKC complexes from 11 embryos (S71A); n = 676 total CDC-42/aPKC complexes from 5 embryos (S71E). Orange bars are measurements of k_{off} for the complex of wild-type mNG::CDC-42 and PAR-6 during polarity establishment or polarity maintenance (Deutz et al., 2023), shown here for comparison. See also Fig. S4.

Thus far our data suggests that phosphorylation of CDC-42 on S71 weakens the interaction between CDC-42 and Par-6/aPKC. This could explain why the CDC-42 phosphomimetic mutant loses its asymmetric localisation. Moreover, the release of aPKC upon phosphorylation of CDC-42 could lead to aPKC recruitment by PAR-3, thereby promoting the asymmetric localisation of aPKC. Hence, we decided to analyse the localisation of PAR-3 and aPKC in the CDC-42 phosphomutants to determine how the destabilisation or stabilisation of CDC-42/aPKC association can alter aPKC localisation in relation to PAR-3.

In mid-plane images of the plasma membrane focusing at the end of the aPAR domain, a CDC-42 dependent expansion of aPKC relative to PAR-3 can be detected (**Fig. 3A**, grey double head arrow and **Fig.3B & C**). Because this expansion depends on CDC-42 and not on PAR-3, its extent can be used as a measure of the abundance of CDC-42/PAR-6/aPKC complex at the membrane.[36] We observed that in the CDC-42(S71E) mutant, this expansion was absent and that aPKC localisation matched that of PAR-3 (**Fig. 3B & C**). Cortical sections of CDC-42(S71E) zygotes also showed this increased co-localisation of aPKC with PAR-3 and enhanced aPKC asymmetry (ASI index) (**Fig. 3D-F**). Moreover, we found that in CDC-42(S71E) zygotes aPKC presented an increased clustered organisation (analysed by the coefficient of variance, CV) (**Fig. 3G**), more typical of PAR-3.[36]These results indicate that the membrane localisation of PAR-6/aPKC in the CDC-42(S71E) mutant depends primarily on PAR-3. We observed a similar dependency when CDC-42 is depleted by RNAi (**Fig. 3E-G**). In the CDC-42(S71A) mutant the CDC-42-dependent expansion of aPKC relative to PAR-3 was larger compared to that observed in wild type (**Fig. 3B & C**), indicating a stabilisation of the CDC-42/PAR-6/aPKC complex at the membrane (**Fig. 3A**). This expansion became more apparent in cortical sections, showing a more homogenous and less clustered population of aPKC, expanding towards the posterior in the domain where PAR-3 is absent (**Fig. 3D-G**). Moreover, when we analysed the co-localisation of aPKC and PAR-3 in the anterior domain, where they overlap, we observed a lower co-localisation index for CDC-42(S71A) compared to wild-type CDC-42 and CDC-42(S71E) (**Fig. 3E**). These results show that the disruption of the CDC-42/PAR-6/aPKC complex by phosphorylation of CDC-42 on S71 leads to increased co-localisation of PAR-3 and aPKC. Conversely, stabilisation of the CDC-42 complex by preventing S71 phosphorylation decreases aPKC co-localisation with PAR-3. These data further support previous work indicating that PAR-3 and CDC-42 compete for PAR-6/aPKC membrane recruitment.[21,80] Overall, our findings suggest that phosphorylation of CDC-42 on S71 through disruption of CDC-42/PAR-6/aPKC complex can mediate the proposed exchange of PAR-6/aPKC from CDC-42 to PAR-3, where aPKC becomes asymmetrically localised.[36] Therefore, we propose that, through CDC-42 S71 phosphorylation, aPKC can promote its own asymmetric localisation.

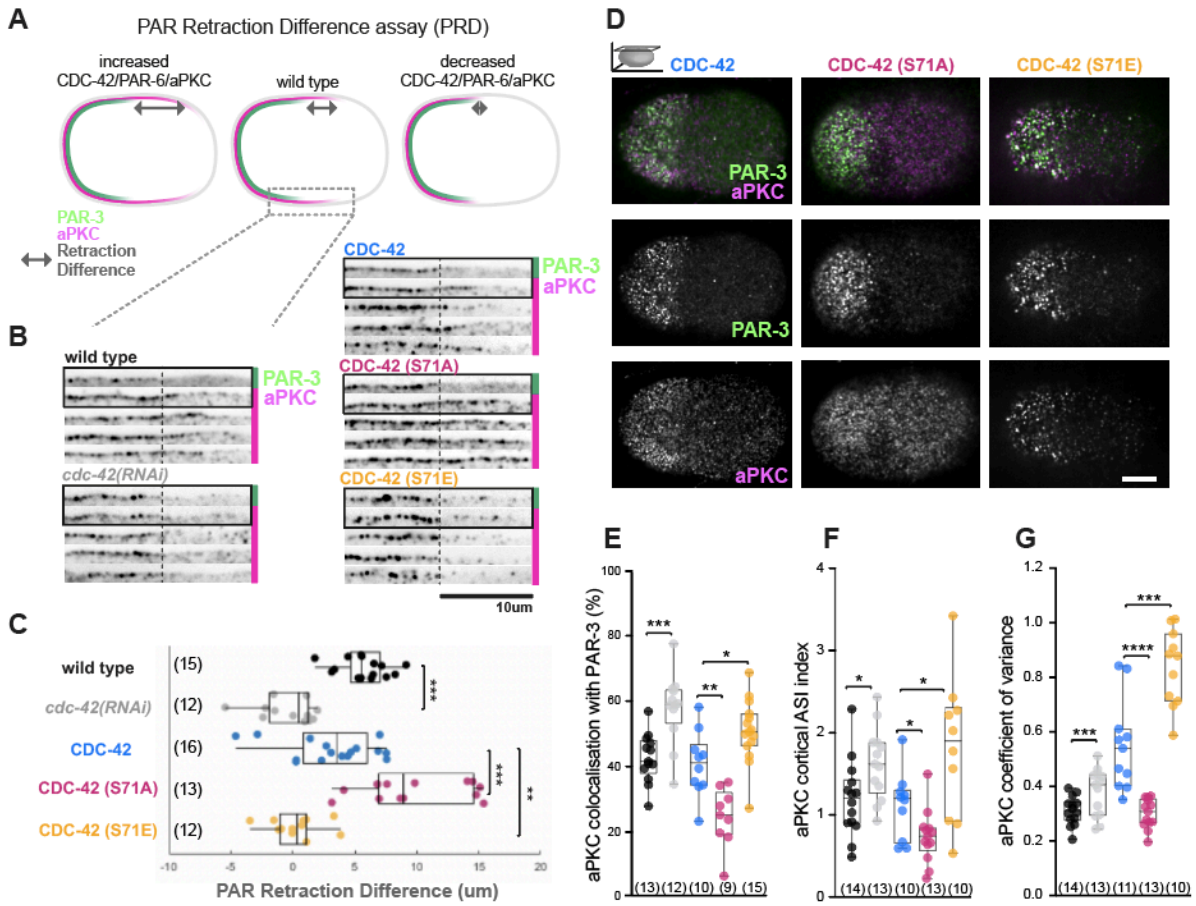

Figure 3. Preventing CDC-42 phosphorylation at serine 71 leads to aPKC cortical expansion. A. PAR retraction difference assay showing zygote phenotypes that indicate an increase or decrease in the CDC-42/PAR-6/aPKC membrane domain that is independent from PAR-3. **B.** Representative flattened membranes from PAR-3 and aPKC co-immunostained zygotes, showing the difference in retraction observed between PAR-3 and aPKC in wild type, *cdc-42* depleted (RNAi of its 3' UTR), GFP::CDC-42, GFP::CDC-42(S71A) and GFP::CDC-42(S71E) strains (in all CDC-42 reporters endogenous CDC-42 is depleted). Four cortices are shown for each strain. PAR-3 and aPKC are shown for the first zygote in each strain. For the other zygotes only aPKC is shown but its position is relative to the end of its corresponding PAR-3 domain (dashed vertical line). **C.** Quantification of PAR retraction difference. S71A mutation in CDC-42 promotes the CDC-42/PAR-6/aPKC membrane domain (as shown by the larger expansion of aPKC relative to PAR-3), whereas S71E mutation decreases membrane CDC-42/PAR-6/aPKC. **D.** Representative cortical confocal images of PAR-3 and aPKC in the indicated CDC-42 strains. In cortical sections we have analysed aPKC and PAR-3 co-localisation (**E**), aPKC asymmetry using ASI index (normalised against wild-type asymmetry, see methods) (**F**) and aPKC coefficient of variance as a means to measure clustered (closer to 1) vs. diffusive state (closer to 0) (**G**). All box plots show the median ± IQR and all data points. Number of embryos analysed indicated in the graphs. Unpaired, two-tail Student's T test *p<0.05 **p<0.01, ***p<0.001, ****p<0.0001. Scale bar: 10 µm.

Phosphorylated CDC-42 is found in anterior cortical foci that depend on aPKC activity and actomyosin organisation

Our data thus far suggests a dynamic mechanism by which the turnover of CDC-42 phosphorylation at S71 determines aPKC association with CDC-42 or PAR-3 and, as a result, regulates aPKC asymmetry. Given that CDC-42 is a small GTPase well known for regulating the actin cytoskeleton,[81,82] we also wanted to determine if this phosphorylation had a role in the organisation of the actomyosin cortex and, in this way, could also regulate aPKC asymmetry. Staining with a phospho-specific antibody against CDC-42 phospho-S71 (CDC-42 pS71) revealed an enrichment of phosphorylated CDC-42 at cortical foci in the anterior half of wild-type zygotes. These foci closely resemble the actomyosin foci that underlie the zygote's membrane during polarity establishment (**Fig. 4A & C**). Upon RNAi knockdown of CDC-42 or mutation of CDC-42 to a non-phosphorylatable form (S71A), we did not detect staining of these cortical foci (**Fig. 4A & B**), supporting the specificity of CDC-42 pS71 detection. Furthermore, knock-down of *C. elegans* homologues of Rac1, which can also be phosphorylated at this conserved site,[71,72,83] did not lead to reduction in pS71-staining (**Fig. S5 A & B**). Note that we did not observe cortical foci of total CDC-42 using the GFP::CDC-42 reporter. This could indicate that only a minority of CDC-42 is in this phosphorylated and focally-localised state. Moreover, we also did not observe the phosphomimetic reporter of CDC-42 (GFP::CDC-42(S71E)) in foci, this could indicate that the phosphomimetic reporter does not mimic perfectly the phosphorylated state of CDC-42. For example, the accumulation of CDC-42 pS71 at such foci might require prior stabilisation of CDC-42 at the membrane in the non-phosphorylated state, which is impeded in the phosphomimetic mutant (**Fig. 1 D-F**).

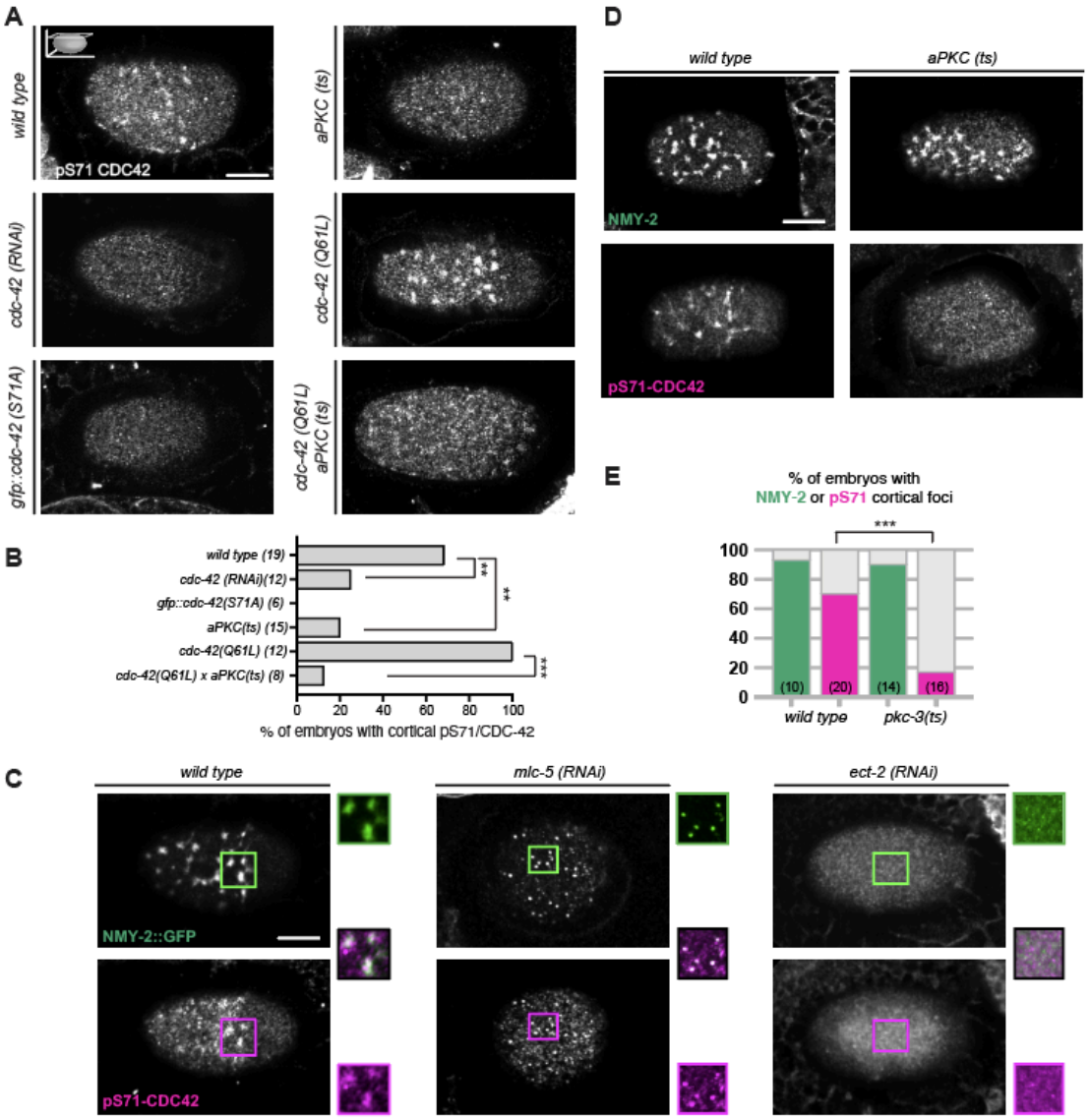

Figure 4. aPKC activity promotes anterior cortical foci of CDC-42 pS71 that co-localise with and depend on myosin foci. A. Immunofluorescent detection of CDC-42 phosphorylation on serine 71 in polarity establishment zygotes, showing the presence or absence of cortical foci in the conditions tested. **B.** Quantification showing the percentage of zygotes with CDC-42 pS71 cortical foci inferred from 2D intensity correlation analysis (see methods). CDC-42 pS71 cortical foci are absent from the cortex upon mutation of the CDC-42 S71 phosphorylation site to alanine (endogenous CDC-42 is depleted in this strain) and are strongly reduced upon inhibition of aPKC kinase activity. **C.** Confocal images of wild-type and *aPKC(ts)* zygotes at establishment, showing the presence or absence of NMY-2 and CDC-42 pS71 cortical foci. **D.** Quantification of NMY-2 and CDC-42 pS71 foci presence in wild-type and *aPKC(ts)* establishment zygotes. Although *aPKC(ts)* embryos show clear cortical NMY-2 foci we observe a clear reduction in CDC-42 pS71 foci compared to wild type. **E.** Representative cortical confocal images of polarity establishment wild-type zygote and zygotes where the actomyosin cytoskeleton is perturbed (*mlc-5* or *ect-2 RNAi*), co-stained for NMY-2 and CDC-42 pS71. Insets highlight the partial co-localisation of CDC-42 pS71 with NMY-2 in the indicated areas (green and magenta squares). Number of embryos analysed indicated in the graphs. Chi-square test **p<0.01, ***p<0.001. Scale bar: 10 µm. See also Fig. S5.

To address if CDC-42 phosphorylation depends on aPKC *in vivo*, we examined CDC-42 pS71 foci upon aPKC knockdown (*aPKC(RNAi)*) or in a temperature sensitive kinase-inactive aPKC mutant (*pkc-3 (ts)).*[36] Under these conditions, we observed a strong reduction in the detection of CDC-42 pS71 foci (**Fig. 4A & B and Fig. S5 A & B**), indicating that CDC-42 phosphorylation depends on aPKC activity in the zygote. Furthermore, CDC-42/GTP has been proposed to promote aPKC activity[14,19,36,37] and, in agreement with this, we found that the constitutively active mutant of CDC-42, CDC-42(Q61L), which favours its GTP state, exhibited more prominent CDC-42 pS71 foci that are dependent on aPKC activity (as seen in *cdc-42(Q61L)* and in *cdc-42(Q61L); aPKC(ts)* strains, **Fig. 4A & B**). In other systems, Akt kinase can phosphorylate small GTPases in this conserved site.[83] However, depletion of the *C. elegans* homologues (AKT-1 and AKT-2), did not lead to a reduction in the pS71-foci staining in the zygote (**Fig. S5 A & B**). Overall, these data show that aPKC promotes CDC-42 phosphorylation on S71 and that, in the *C.elegans,* zygote, this phosphorylation is enriched in anterior cortical foci during polarity establishment.

Given their resemblance, we investigated if CDC-42 pS71 foci depend on the presence of non-muscle myosin II (NMY-2) foci. We first observed that cortical foci of NMY-2::GFP and immunostained CDC-42 pS71 partially co-localised in the zygote (**Fig. 4C**). Both types of foci were observed during polarity establishment and disappeared during polarity maintenance (**Fig. S5 C**). In addition, we observed that cortical localisation of CDC-42 pS71 followed that of NMY-2 when we alter the organisation of the actomyosin cortex. RNAi knockdown of the myosin essential light chain, MLC-5, leads to the condensation of NMY-2 foci into tight immobile puncta that do not disassemble. This configuration prevents the retraction of the actomyosin network to the anterior, with the myosin puncta observable throughout the zygote.[84] CDC-42 pS71 staining in *mlc-5(RNAi)* zygotes co-localised with these NMY-2 puncta (**Fig. 4C**). Consistently, down regulation of the RHO pathway through depletion of the Rho guanine nucleotide exchange factor ECT-2 led to the disappearance of NMY-2[51,52] and CDC-42 pS71 foci (**Fig. 4C**). Note that for these co-localisation analyses we needed to immunostain CDC-42 pS71 in a strain carrying endogenously tagged NMY-2::GFP, where we found the staining of CDC-42 pS71 not as strong as when we stained wild-type zygotes (N2). However, even in wild-type embryos independently immunostained for NMY-2 or CDC-42 pS71 we observed the same relationship, where upon different alterations of the actomyosin cortex, CDC-42 pS71 foci resembled the organisation of NMY-2 foci (**Fig. S5 D**).

Because of the dependency of CDC-42 pS71 foci on NMY-2 foci organisation and the fact that anterior PARs regulate the actomyosin cortex during polarity establishment,[50,85] we questioned the following: is CDC-42 pS71 foci staining dependent on aPKC activity because of a possible role of aPKC on NMY-2 foci formation. However, we found that NMY-2 foci were present upon loss of aPKC activity (aPKC*(ts))* (**Fig. 4D and E**), indicating that the loss of CDC-42 pS71 foci that we observed in *aPKC(ts)* was not due to lack of NMY-2 foci, but most likely due to loss of CDC-42 phosphorylation on S71. Moreover, the CDC-42(S71A) strain, where we do not detect CDC-42 pS71 staining, presented very clear and defined NMY-2 foci (**Fig. 5 A & B**). Overall, these results indicate that aPKC-mediated phosphorylation of CDC-42 is enriched at actomyosin cortical foci during polarity establishment.

CDC-42 phosphorylation on serine 71 impacts the organisation of the actomyosin cortex

Given that CDC-42 pS71 localises to actomyosin foci, we next asked if this phosphorylation is important for regulation of the actomyosin cortex. In the *C. elegans* zygote, the cortex is a highly contractile network of actomyosin foci, interlaced by actin filaments, that retracts or 'flows' toward the anterior of the zygote during polarisation.[50,86,87] These actomyosin foci exhibit a pulsatile behaviour undergoing assembly, growth, shrinkage and disassembly.[53,54] Studying the localisation of endogenously tagged NMY-2 (NMY-2::mKate2) in the CDC-42 phosphomutants we observed that, during polarity establishment, the actomyosin cortex is altered. NMY-2 foci were still present in both mutants, but in non-phosphorylatable CDC-42(S71A) zygotes, these foci were better delineated than those observed in control CDC-42 zygotes (**Fig. 5A**). We quantified this difference by measuring the coefficient of variation (CV) of NMY-2 intensity in the anterior cortex, where a higher CV is representative of a cortex with well-defined clustered foci, whereas a lower CV represents relatively uniform distribution of NMY-2. We observed that CDC-42(S71A) had a higher CV than CDC-42 (**Fig. 5B**). Note that we observed a similar trend upon depletion of *cdc-42*, presenting better-defined NMY-2 foci when compared to wild-type zygotes (**Fig. 5A & B**). This suggests that CDC-42 reduces de organisation of actomyosin foci and that preventing CDC-42 phosphorylation impedes this function. In accordance with this result, the phosphomimetic CDC-42(S71E) presented ill-defined NMY-2 foci, with lower CV than CDC-42 (S71A) (**Fig. 5A & B**). Wild-type CDC-42 exhibited an intermediate median value between CDC-42(S71A) and CDC-42(S71E). Note that the observed NMY-2 foci alterations led to changes in the actomyosin cortical flow measured in the antero-posterior axis (AP flow) (**Fig. 5C & D**), indicating that either too clustered or loose NMY-2 foci can affect AP flow velocities (**Fig. 5E**). This suggests that CDC-42 phosphorylation levels need to be controlled to enable adequate actomyosin cortex organisation and cortical flow speed.

At a later stage, during polarity maintenance, the actomyosin network of connected actomyosin foci disassembles and NMY-2 is observed as homogenously distributed puncta enriched at the anterior (**Fig. 5F**). CDC-42 is required for the cortical recruitment of NMY-2 during this stage.[50–52,67,69] Therefore, we decided to investigate if CDC-42 phosphorylation could be regulating actomyosin cortex organisation during polarity maintenance. We observed that, in CDC-42(S71E) mutants the cortical localisation of NMY-2 is strongly reduced, similar to that observed upon depletion of CDC-42 (**Fig. 5F & G**), suggesting that CDC-42 phosphorylation prevents CDC-42 function during polarity maintenance. In agreement with this, CDC-42(S71A) zygotes, NMY-2 presents an asymmetric cortical localisation very similar to that observed in wild-type zygotes.

In summary, our data shows that CDC-42 regulates the organisation of the actomyosin cortex during polarity establishment and maintenance. During polarity establishment, CDC-42 is involved in the organisation of actomyosin foci, its phosphorylation possibly promoting actomyosin foci turnover. At maintenance stage, CDC-42 phosphorylation prevents CDC-42 mediated cortical recruitment of NMY-2.

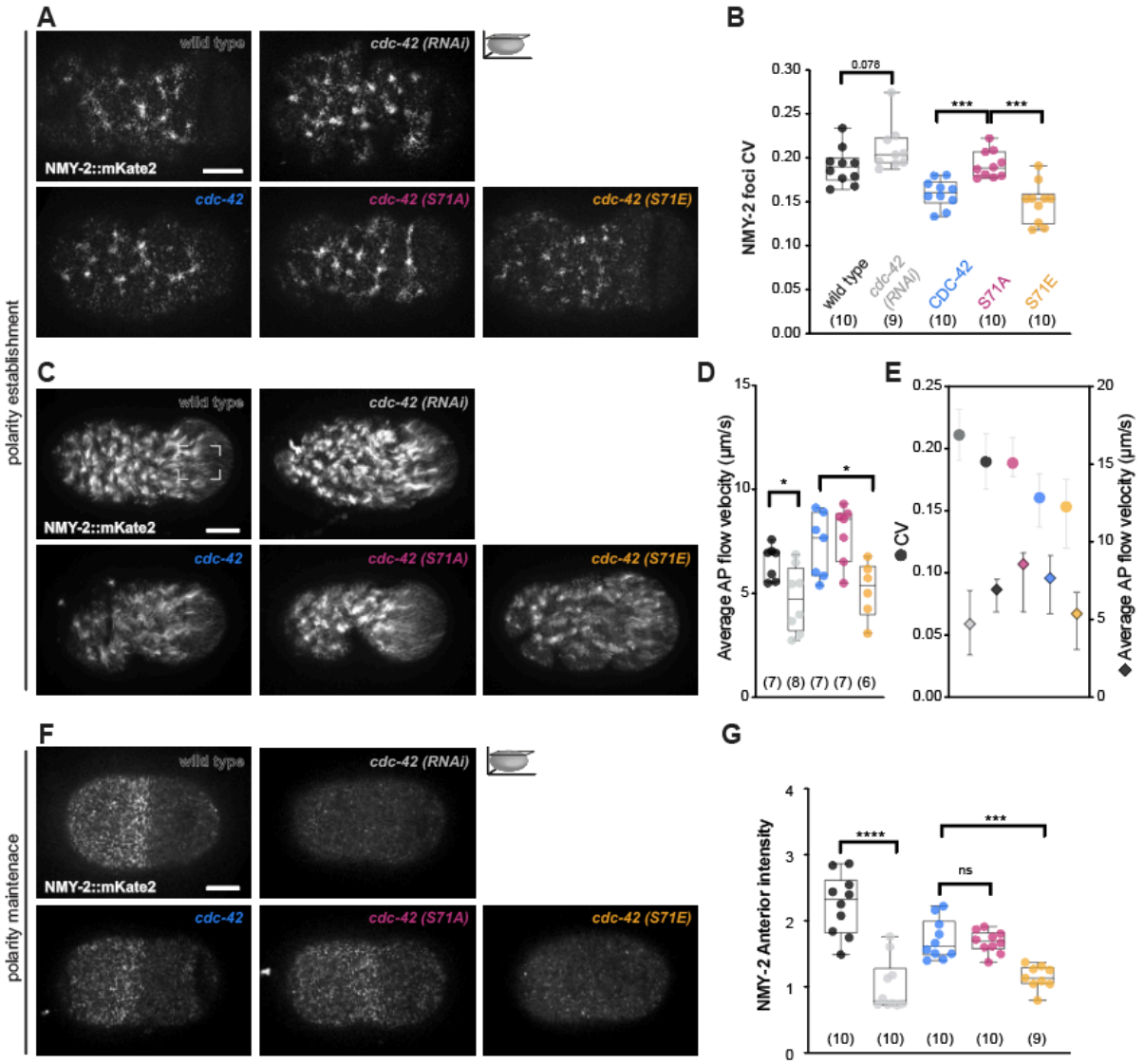

Figure 5. Phosphorylation of CDC-42 is required for CDC-42-dependent disorganisation of actomyosin foci during polarity establishment. However, CDC-42 phosphorylation prevents CDC-42 mediated cortical recruitment of NMY-2 during polarity maintenance. A. Representative cortical confocal images of NMY-2 in establishment wild-type, *cdc-42* depleted, CDC-42, CDC-42(S71A) and CDC-42(S71E) zygotes. In all CDC-42 reporter lines endogenous CDC-42 is depleted. **B.** Graph showing the coefficient of variation (CV) as a measurement of myosin cortex organisation. Well-defined foci lead to higher CV values, whereas a dispersed appearance leads to lower values. **C.** Representative time projections (100 frames) of NMY-2 confocal cortical images during actomyosin flow in polarity establishment zygotes, showing the actomyosin cortex clearance from the posterior in the different conditions. **D.** Comparison of average AP flow velocity in the posterior of embryos (representative area studied for AP flow measurements highlighted in wild type) for the specified conditions. **E.** Co-plotting of CV (higher to lower from left to right) and NMY-2 flow for ease of comparison. Showing median ± CI 95%. **F.** Representative cortical confocal images of NMY-2 in maintenance (prior to cleavage furrow) wild-type, *cdc-42* depleted, CDC-42, CDC-42(S71A) and CDC-42(S71E) zygotes. In all CDC-42 reporter lines endogenous CDC-42 is depleted. **G.** NMY-2 intensity at the anterior half of the zygote normalised by its intensity at the posterior during polarity maintenance. All box plots show median ± IQR and all data points. Unpaired, two-tail Student's t-test *p<0.05, ***p<0.001, ****p<0.0001, ns not significant. Scale bar: 10 µm.

DISCUSSION AND MODEL

In previous work, we proposed that aPKC activity and localisation depend on a dynamic cycle of PAR-6/aPKC shuttling between PAR-3 and CDC-42 (aPKC cycle, **Fig. 6**). In complex with PAR-3, PAR-6/aPKC become anteriorly localised by the actomyosin flow whereas, in complex with CDC-42, aPKC becomes active.[36] Here, we describe how aPKC can promote its own asymmetric localisation by controlling the aPKC cycle between these complexes (**Fig. 6**). Our results indicate that aPKC-dependent phosphorylation of CDC-42 (**step 1** in **Fig.6**) leads to both reduced CDC-42 membrane binding and the dissociation of aPKC from CDC-42, thus promoting the membrane localisation of aPKC via PAR-3, and hence aPKC asymmetry. Moreover, we observed phosphorylated CDC-42 enriched at cortical actomyosin foci where CDC-42 could be regulating the dynamics of these foci.

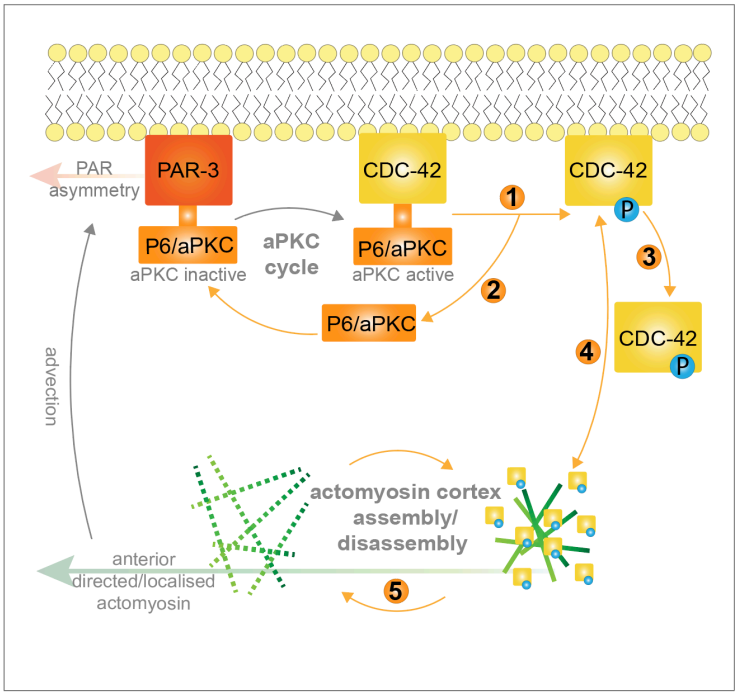

Figure 6. Model for aPKC self-patterning through phosphorylation of CDC-42. aPKC phosphorylation of CDC-42 (**step 1**, Fig.1A & C and Fig.4A & B), leads to aPKC release through CDC-42/aPKC dissociation (**step 2**, Fig. 2). Released aPKC can then associate with PAR-3 clusters (Fig. 3E), which promote aPKC asymmetry. CDC-42 phosphorylation reduces CDC-42 cortical localisation (**step 3**, Fig.1D-F), which is then stabilised at actomyosin foci (**step 4**, Fig. 4). Turnover of CDC-42 phosphorylation is needed for the correct actomyosin cortex organisation. Phosphorylation of CDC-42 leads to actomyosin cortex disassembly by promoting CDC-42 function during polarity establishment or by inhibiting CDC-42 function during polarity maintenance (**step 5**, Fig. 5).

Our research indicates that aPKC-dependent phosphorylation of CDC-42 on S71 disrupts the CDC-42/PAR-6/aPKC complex (**step 2**). PAR-6 and aPKC are thought to interact with CDC-42 via the PDZ and semi-CRIB domains of PAR-6.[16,18,19,37,88,89] Phosphorylation of S71, which is positioned between the effector protein-binding and the GTP-binding domains of CDC-42,[90] is known to disrupt the interaction of CDC-42 with N-WASP and PAK1.[72] We speculate that, in a similar way, S71 phosphorylation could disrupt the interaction between

CDC-42 and PAR-6. Alternatively, aPKC might make direct interactions with CDC-42 that contribute to stable assembly of a CDC-42/PAR-6/aPKC complex and are released upon completion of aPKC's catalytic cycle. Similar aPKC "substrate phosphorylation and release" mechanisms have been proposed for other aPKC polarity targets. In epithelial cells phosphorylation of Par3 by aPKC weakens the association between Par3 and aPKC, and excludes Par3 from the apical membrane.[27,35,91–93] In the *Drosophila* neuroblast, phosphorylation of LGL by aPKC also leads to the dissociation of LGL from Par6/aPKC.[34,94] In the *C. elegans* zygote, LGL phosphorylation is thought to mediate the release of the whole PAR-6/aPKC/LGL complex from the membrane in a process described as "mutual elimination".[66] The aPKC expansion we observed in the non-phosphorylatable CDC-42 mutant indicates that a similar mechanism could exist for CDC-42/PAR-6/aPKC, in this case for "self-elimination". For the "substrate phosphorylation and release" mechanism to take place aPKC should be able to access and phosphorylate the CDC-42 it is forming a complex with. Structural information of the CDC-42/PAR-6/aPKC complex is required to determine if this mechanism is possible. Alternatively, aPKC in complex with CDC-42/PAR-6 could be accessing other CDC-42 molecules in the vicinity.

CDC-42 is known to promote aPKC activity and diffusion at the membrane,[14,19,36,37,39] hence aPKC-mediated dissociation of CDC-42 and aPKC through phosphorylation of CDC-42 could constitute an aPKC negative feedback mechanism. This negative feedback would not only restrict aPKC activity but also its domain of action by promoting aPKC association with PAR-3. aPKC could turn itself off by destabilising the CDC-42 complex it resides in, or alternatively aPKC phosphorylation of nearby CDC-42 molecules would prevent other aPKC molecules to become activated by impeding their stable interaction with CDC-42. Our measured k_{off} of 0.100 s^{-1} for the CDC-42(S71E)/aPKC complex suggests an average lifetime of ~7 seconds for these complexes once phosphorylation occurs, compared to ~12 seconds for the unphosphorylated complex (k_{off} = 0.060 s^{-1}). Depending on the catalytic rates of active aPKC, these lifetimes could still be adequate to allow aPKC to phosphorylate other substrates, especially those that are kinetically more favourable, accessible or abundant than CDC-42.[38] It is noteworthy that CDC-42 does not present an optimal aPKC consensus site (**Fig. 1B**), so other aPKC substrates could be more efficiently phosphorylated. We have previously reported *ex vivo* kinetic measurements that suggest CDC-42/aPKC complexes are more stable during polarity maintenance (k_{off} = 0.050 s^{-1}, lifetime ~14 sec) than establishment (k_{off} = 0.109 s^{-1}, lifetime ~6 sec).[80] Strikingly, the phosphomimetic and non-phosphorylatable mutants of CDC-42 exhibited CDC-42/aPKC lifetimes similar to those observed in establishment and maintenance, respectively. Although only a correlation and we acknowledge that other factors could be in place, our data suggests that the phosphorylation of CDC-42 is regulated differently between establishment and maintenance. We do not know the underlying mechanisms, but differential regulation of aPKC activity or different availability of competing substrates or interactors could be involved.[21,38]

aPKC is known to inhibit the association of some of its substrates with the membrane by phosphorylating and neutralising residues in short polybasic hydrophobic sequences (BH motifs) involved in membrane targeting.[95,96] However, the CDC-42 S71 residue is not present in a BH motif (analysed using the BH scoring algorithm[97]); and, moreover, membrane localisation of CDC-42 depends mostly on C-terminal polybasic residues and a prenylated cysteine.[23,25,98,99] Therefore, it is unlikely that S71 phosphorylation regulates the membrane localisation of CDC-42 in this way. We propose that S71 phosphorylation

destabilises CDC-42 membrane localisation and asymmetry (**step 3**) through disruption of CDC-42 interaction with PAR-6/aPKC or with other CDC-42 partners. This idea is supported by the positive feedback described in *Drosophila* neuroblast and in the *C. elegans* zygote, where PAR-6 promotes robust membrane localisation of CDC-42 (**Fig. S2**).[14,69] PAR-6/aPKC could stabilise CDC-42 at the membrane by providing additional membrane contact sites, for example the recently identified polybasic domain of aPKC that is capable of targeting PAR-6/aPKC to the plasma membrane.[29,30]

The reduced membrane binding of the phosphorylated state of CDC-42 (**step 3**) and its enrichment at actomyosin foci (**step 4**), suggests that phosphorylated CDC-42 interacts in some way with the actomyosin cortex. We do not know if the phosphorylated state of CDC-42 is recruited to actomyosin foci or alternatively stabilised at the membrane by these foci (indicated by **step 4** double arrow). These processes could be mediated by known interactions of CDC-42 with actomyosin regulators. [81,82,100] Interestingly, aPKC phosphorylation-dependent recruitment of proteins to the actomyosin cortex has also been proposed in the *Drosophila* neuroblast. Here, the scaffold protein Miranda, involved in the subcellular distribution of cell-fate determinants, is phosphorylated by aPKC. This leads not only to Miranda release from the apical membrane, where aPKC resides, but also to the basal recruitment of Miranda to a specific domain of the actomyosin cortex.[101] aPKC-driven recruitment of polarity effectors to certain actomyosin cortex domains might be an emerging mechanism in the creation of cellular asymmetries and it could also provide aPKC with the means to control actomyosin cortical dynamics.

The localisation of phosphorylated CDC-42 to actomyosin foci and the identified role for CDC-42 in actomyosin foci organisation (**step 5**) is intriguing. There is a clear regulatory feedback between PARs and the actomyosin cortex during polarity establishment,[50,51,85] but the molecular mechanism remains unknown. Our results suggest that aPKC-dependent phosphorylation of CDC-42 may be an important regulation of this feedback mechanism. During polarity establishment the actomyosin cortex is heavily controlled by RhoA (RHO-1 in *C. elegans*) signalling, driving its anterior directed movement (flow) and orchestrating the pulsatile behaviour, assembly and disassembly, of actomyosin foci.[53,54] Our data suggests that CDC-42 and the control of its phosphorylation levels are also important for the correct actomyosin foci organisation and flow. This supports a role for CDC-42 during polarity establishment,[51,55] in addition to its well-known function during polarity maintenance where we found that, phosphorylation of CDC-42 prevents it from mediating the asymmetric cortical localisation of NMY-2.[50–52,67,69] We do not know how CDC-42 phosphorylation is regulating the actomyosin cortex of the zygote, it could be through regulation of CDC-42 interaction with and activation of downstream targets, such as aPKC/PAR-6 (reported here) and actomyosin regulators (e.g MRCK, PAK, N-WASP, WASP). Further work is needed to fully understand how aPKC-dependent phosphorylation of CDC-42 regulates actomyosin dynamics.

Overall, our work shows that one aPKC output, CDC-42 phosphorylation, regulates two processes that impact the asymmetric localisation of the conserved polarity factors PAR-3, PAR-6/aPKC and CDC-42. Firstly, CDC-42 phosphorylation regulates PAR protein organisation at the membrane, promoting PAR-6/aPKC release from CDC-42 and in turn PAR-6/aPKC membrane loading onto PAR-3 clusters, where PAR-6/aPKC become asymmetrically localised by coupling to the actomyosin flow. Secondly, the turn-over of

CDC-42 phosphorylation regulates the dynamics of the actomyosin cortex involved in PAR asymmetry. In both of these instances, CDC-42 phosphorylation acts as a molecular switch whereby the phosphorylated and dephosphorylated states regulate molecular cycles: aPKC shuttling between PAR-3 and CDC-42, and the assembly/disassembly of the actomyosin cortex. aPKC-dependent phosphorylation of CDC-42 is likely to be a conserved mechanism coordinating PAR complex formation, aPKC activity and actomyosin dynamics. aPKC and CDC-42 have widespread roles in cell polarisation and phosphorylation of CDC-42 on S71 has been observed in other polarising cells, for example at the leading edge of migrating cells.[73] Therefore, we predict that the identified aPKC-self regulatory feedback will be a widely conserved mechanism ensuring the robust polarisation of cells.

METHODS

***C. elegans* strains and maintenance:** The strains used in this study are listed in strain table (key resources table). All strains were maintained on nematode growth media (NGM) under standard conditions.[102] Temperature sensitive strain *pkc-3(ne4246)* was maintained at 15 °C and shifted to 25°C for aPKC inactivation. The rest of reporter the strains were maintained at 25 °C.

***C. elegans* transgenic animals**: Strains expressing GFP::CDC-42 (JRL1685), GFP::CDC-42(S71A) (JRL1686) and GFP::CDC-42(S71E) (JRL1687) constructs were generated for this study with the Mos-1 mediated single copy transgene insertion method (MoSCI).[103,104] Genomic cdc-42 was amplified from genomic worm extract using the following primers (fwd: ggggacaagtttgtacaaaaaagcaggctcgatgcagacgatcaagtgc; rev: ggggaccactttgtacaagaaagctgggtctagagaatattgcacttcttcttct) and inserted into the pDONR221 plasmid (#12536017, Invitrogen) using the BP clonase II enzyme (#11789100, Invitrogen) to generate pDONR221- gCDC42attb. The plasmid was introduced by heat shock into DH5alpha and extracted with standard Miniprep (#K0503, ThermoFisher). The S71A and S71E mutations were introduced into the pDONR221- gCDC42attb plasmid with the QuickChange II XL Site directed mutagenesis kit (#200521, Agilent technologies) with the following primers, fwd S71A: gatcgattaaggcctcta**gcc**tatccacagaccgacgtg; rev S71A: cacgtcggtctgtggata**ggc**tagaggccttaatcgatc; fwd S71E: cgatcgattaaggcctcta**gag**tatccacagaccg acgtc; rev S71E: cacgtcggtctgtggata**ctc**tagaggccttaatcgatcg. The resulting plasmids were inserted into XL10-Gold ultracompetent cells (#200314, Agilent) via heat shock as indicated by the provider and extracted with standard Miniprep (#K0503, ThermoFisher). The resulting plasmids were used in an LR reaction (Gateway LR clonase II enzyme mix, # 11791-020 ThermoFisher) with plasmids pCFJ210 (#30538 Addgene), pJA245 #21506 Addgene), pCM1.36 (#17249 Addgene). This reaction created a plasmid for MoSCI insertion in chromosome I (4348) containing mex-5 promoter and GFP sequence at the N-term of cdc-42, and tbb-2 3'UTR at its C-term. The resulting plasmid was co-injected with the pie-1 promoter transposase (pCFJ103),[104] and two fluorescent reporters (pCFJ04, pCFJ90) into the gonad of young adult worms presenting *unc-119(ed3);ttTi4348 genotype* (EG6701 strain, CGC). Wild type moving worms without red fluorescence were selected for sequencing, to confirm the presence of the desired construct.

Bacterial Strains: OP50 bacteria were obtained from CGC. Feeding by RNAi was performed with HT115(DE3) bacteria strains containing the indicated RNAi plasmid from the Ahringer library[105] (key resources table). The RNAi clone that targets the 3'UTR of CDC-42 was generated through amplification of genomic CDC-42 3'UTR (Fwd: gaagatctgaacgtcttccttgtctccatgt; Rev: ggggtaccacgtaacggtgtatccggac) and insertion into the L4440 plasmid (#1654 Addgene). Control bacteria is transformed with empty L4440 vector (#1654 Addgene).

***C. elegans* - RNAi Feeding**: HT115(DE3) RNAi clones were inoculated from LB-agar plates (10 µg/ml of carbenicillin, 10 µg/ml tetracycline, 100 U/ml nystatin) into 5 ml LB liquid cultures (10 µg/ml of carbenicillin, 10 µg/ml tetracycline, 100 U/ml nystatin) and grown over night at 37°C. The bacteria were induced for 4 h with 4 mM IPTG at 37 °C with agitation and concentrated five-fold before seeding 300 µl of the bacterial culture onto NGM plates (10

µg/ml of carbenicillin, 10 µg/ml tetracycline, 1mM IPTG, 100 U/ml nystatin). For partial depletion of *par-6*, bacteria expressing the desired clone was mixed at the indicated ratio with bacteria expressing control RNAi. L4 larvae were added to RNAi feeding plates and incubated for 72 h at 15 °C. For temperature sensitive *pkc-3(ne4246)* line, the worms were shifted to 25 °C for 2 h before fixing or imaging.

***In vitro* – aPKC Kinase Assays**: *In vitro* kinase assays were performed in the presence or absence of different recombinant human atypical PKC (50 or 100 ng of PKC ζ, #14-525 Merk Millipore; 1µg of PKC I/αPar6 complex, gift from Shona Ellison, Mc Donald lab, Crick Institute) and with different recombinant Cdc42 (3µg of human Cdc42, #CD01 Cytoskeleton; 3µg of recombinant MBP tagged- *C. elegans* CDC-42 or CDC-42(S71A)), which were incubated for 1 hour at 30 °C in 30 µl kinase-assay buffer (25 mM Tris pH 7.5, 25 mM NaCl, 5 mM MgCl2, 0.5 mM EGTA, 1 mM DTT) containing 1mM ATP-gamma-S (# ab138911,Abcam). The phosphorylation reaction was stopped with 10mM EDTA, followed by alkylation for one hour at room temperature with 1.5 mM PNBM (p-nitrobenzyl mesylate, #ab138910 Abcam). Reactions were stop in 1x Laemmli buffer at 95 °C for 5min. Samples were processed for Western-blot and phosphorylation was detected using an anti-thiophosphate ester antibody (#ab92570, Abcam).

***In vitro* – Purification of CDC-42 recombinant proteins**:
MBP::CDC-42 and MBP::CDC-42(S71A) recombinant proteins were generated for this study Briefly, MBP::CDC-42 coding sequence was inserted into the pMAL-c5X plasmid (NEB). The S71A mutation was introduced into the pMALc- MBP::CDC-42 plasmid with the QuickChange II XL Site directed mutagenesis kit (#200521, Agilent technologies) with the following primers, fwd S71A: gatcgattaaggcctcta**gcc**tatccacagaccgacgtg; rev S71A: cacgtcggtctgtggata**ggc**tagaggccttaatcgatc. For protein production NEB Express Competent E coli (#C2523H) were transformed with the resulting plasmids. An overnight culture was used to inoculate 500 ml of 2TY medium and grown at 37 ºC until an OD of 0.5 at 600 nm was reached. Then cultures were induced with 0.25 mM IPTG for 19 h at 18 ºC with agitation (210 rpm). Bacteria were lysed with sonication and supernatant obtained after 20.000 xg for 30 min at 4 ºC centrifugation. Supernatant was diluted 1:6 in column buffer (20 mM Tris pH7.4, 0.2 M NaCl, 1 mM EDTA) and passed through an amylose resin column (NEB#E8021L). Columns were washed prior to recombinant protein elution with 10 mM maltose in column buffer.

***C. elegans embryos* – Western Blots**: Embryos were obtained by a standard bleaching protocol and resuspended in NuPAGE LDS sample buffer (Invitrogen) prior to sonication using the Biorupture (Diagenode) for 5 cycles – 30 sec on, 30 sec off. Samples were heated at 70 °C for 10 min before centrifugation at 13000 rpm for 20 min to obtain cleared supernatants. Samples were run on a 12% NuPAGE gel using MOPS SDS running buffer (Invitrogen) and transferred in semi-dry conditions onto PVDF membrane (Immobilon-P membrane 0.45 µm, Millipore). A primary anti-GFP (#11814460001 Roche, 1:1000) was used to detect the different GFP constructs. A primary anti-HSP-60 was used for the loading control (DSHB, P50140 - CH60_CAEEL, 1:1000). Detection of thiophosphate ester tagged proteins from the *in vitro* kinase assay was done with a specific anti-thiophosphate ester antibody (#ab92570 Abcam 1:10000). Antibody against total CDC-42 was use for the loading control (#sc-390210, Santa Cruz 1:1000). Secondary antibodies indicated in the key resources table were used as recommended by provider. The blots were revealed via

chemiluminescence (# GERPN2236 ECL prime, GE Healthcare Life Sciences). Western blot bands were analysed using Fiji image analyses software.

***C. elegans zygote* - Immunofluorescence**: Immunofluorescence was performed as previously described.[106] Briefly, adult worms were collected and washed with M9 buffer (22 mM KH_2PO_4, 42 mM $NaHPO_4$, 86 mM NaCl and 1 mM $MgSO_4$). 30 worms (in 7-10 µl of M9 suspension) were transferred to a microscopy slide (# 10-2066a Erie Scientific) coated with 0.1% poly-lysine. Embryos were released from the adult worms using a needle and then compressed with a coverslip, before being snap-frozen on dry ice for 30 minutes. The coverslip was then removed, and the slide fixed in methanol at room temperature for 30 minutes, following rehydration with PBS (two 10 min washes) and PBS+0.2% Tween-20 (10 minutes) before proceeding with antibody incubation, DAPI staining and Mowiol mounting (#81381 Sigma). All antibodies used are listed in key resources table. Primary antibodies dilutions used: anti-PAR-3 1:50 (# P4A1 Developmental Studies Hybridoma Bank) and anti-PKC-3 1:500 (Tabuse et al., 1998), anti- CDC-42 pS71 1:500 (#44214G Invitrogen), anti-NMY-2 1:25.000 (Ahringer Lab). Secondary antibodies were used as recommended by provider.

Confocal images were capture with a Nikon A1r+ scanning confocal on a Nikon Ni body, equipped with a PlanApochromat 63x 1.4 NA oil-immersion lens. The system presents GaAsP (for green and red channels) and PMTs (for blue and far rad) detectors and runs with Nikon elements software. Cortical immunofluorescence images (**Fig. 3B** & **D**) were captured in a spinning disk with a bespoken 3i system (see specs bellow – live imaging section)

***C. elegans* – Live Imaging**: Embryos were dissected in 4 µl of M9 buffer (22 mMKH2PO4, 42 mMNaHPO4, 86 mM NaCl and 1 mMMgSO4) on top of a 30 mm circular coverslip (#10343435 Fisher Scientific). The coverslip with the dissected worms was then inverted onto 2% agar pads in egg buffer solution (2 mM CaCl2, 118 mM NaCl, 48 mM KCl, 2 mM MgCl2, 25 mM HEPES (pH 7.4)) placed in a custom-made temperature control stage holder (Bioptechs Oasis Cooling System). To gain further sample temperature stability the objective temperature is also controlled with an objective cooling collar (Bioptechs Oasis Cooling System). Sample temperature is normally set at 20 °C unless stated.

Confocal images were capture with a PlanApochromat 100x 1.4 NA oil-immersion lens on a Leica DMRBE (Leica) equipped with an CSU-X1 A1 Spinning Disk Confocal (Yokogawa) and LaserStack v4 Base holding 405, 488, 561 and 640 nm lasers (3i, Intelligent Imaging and Innovation). Images are acquired with a Prime 95B Back illuminated scientific CMOS and the system runs with SlideBook 6 software (3i).

For all live NMY-2::mKate2 imaging; embryos were imaged from early establishment (pronuclear touch) to cytokinesis – to affirm viability. For NMY-2 tracking analyses, embryos were imaged every second with the 560 laser for excitation of mKate2. For GFP::cdc-42 (and S71 mutants) live imaging, embryos had cortical and midplane images taken during maintenance (between pronuclear meet and metaphase).

Single-molecule near-TIRF microscopy in live embryos (HILO)
Imaging was performed on a bespoke single-molecule TIRF microscope constructed around a Nikon Ti-E microscope body, using an Obis 488 laser set to 20 mW, beam expanded to

~20µm and using highly inclined illumination (HILO). Imaging was performed using Photometrics Evolve 512 at 100 nm/pixel with a 100x Nikon 1.49NA TIRF objective lens. Subarraying the camera sensor to a ROI of 128x128 pixels to achieve 15ms/frame exposure time. All images of GFP::CDC-42 and CDC-42 mutant variants were taken of the anterior cortex of maintenance phase embryos (between pronuclear meet and metaphase and for up to 15 s).

Single-cell, single-molecule pull-down in lipid nanodiscs

CDC-42 lipid nanodisc pull-downs were performed exactly as described.[80] Briefly, *C. elegans* nematodes expressing the desired GFP::CDC-42 variant and carrying endogenously tagged HaloTag::aPKC were cultured overnight at 20 ºC in liquid culture containing 15 µM JF_{646} Halo ligand[107] to label the HaloTag::aPKC molecules. Labelled worms were dissected in egg buffer and embryos were rinsed twice with nanodisc buffer (10 mM Tris (pH 8.0), 150 mM NaCl, 1% DIBMA (DIBMA 12 Tris, Cat# 18014 from Cube Biotech), and 0.1 mg/mL bovine serum albumin). A labelled zygote was transferred to a PDMS microfluidic device that had been passivated with PEG, functionalized with anti-GFP nanobodies, and equilibrated in nanodisc buffer. The device was sealed with clear tape and transferred to a custom-built TIRF microscope equipped with a pulsed 1064 nm laser for rapid cell lysis; a 60x, 1.49 NA Olympus TIRF objective; 488 nm and 638 nm lasers for excitation of GFP and JF_{646}, respectively; a home-built 4-color image splitter; and a Photometrics PrimeBSI Express camera.[26] A brightfield image was acquired to document the embryonic stage, and then the embryo was lysed with a single shot from the pulsed laser. Beginning immediately after lysis, TIRF images were collected at 20 frames per second for 500 s to detect binding of GFP::CDC-42 and HaloTag::aPKC molecules to the coverslip. To allow correction of k_{off} values for JF_{646} photobleaching, control experiments were performed on the same days using a transgenically expressed YFP::HaloTag protein to measure JF_{646} photobleaching rates. Images were processed to extract kinetic information as described below.

QUANTIFICATION AND STATISTICAL ANALYSIS

Image analysis- General: Images were analysed with FIJI[108] and MATLAB (Mathworks). Secondary processing of images was performed using Photoshop and Illustrator (Adobe).

Image analysis – Membrane intensity levels: To determine the membrane intensity of aPKC and CDC-42 of immunostained zygotes a 20-pixel wide stripe with the cell membrane at its centre was obtained from straightening the zygotes perimeter from anterior to posterior and back to anterior (custom-built FIJI macro to create cortical flat-outs from midplane images). The flat-out was then read by a custom-built MATLAB script. Each stripe was split in half and two anterior values were obtained per zygote. We analysed the first 20 x 100-pixel band at the anterior domain of each stripe. For each of the 1px columns in this band the average pixel intensity of the highest values encompassing the cortex (10 highest pixels for aPKC and 5 highest for CDC-42) was calculated. The average intensity of the anterior-most domain was then normalised by the cytoplasmic intensity. For CDC-42 this corresponded to the average value intensity of a 10 x 100 pixel band at the anterior most domain but positioned 50 pixels away from the membrane and in the cytoplasm. However, for aPKC because it showed and asymmetric intensity also in the cytoplasm we normalised

aPKC membrane intensity with the average value intensity of a cytoplasmic 10 x 50 pixel band at the posterior most domain (last 50-pixel column band).

For CDC-42 membrane intensity levels from live embryos each stripe was split in half and two values were obtained per zygote for each the anterior and posterior domain. We analysed a 60 x 60 pixel square at the anterior domain of each stripe, this was located 60 pixels away from the anterior pole (leftmost edge of the image) between pixels 60 to 120 in the x axis. For each of the 1 px rows in this band the average pixel intensity was calculated to give an average cross section of (from top to bottom) background-cortex-cytoplasm. The average intensity of the anterior most domain was then normalised by the cytoplasmic intensity. This corresponded to the average value intensity of a 60 x 10 pixel band within the anterior defined area but positioned between 50 and 60 pixels in the y axis (ie. the bottom of the image). Posterior analyses were conducted on the final 60 x 60 pixel region of the halved cortex and had the same cytoplasmic correction applied. Profiles and measurements were averaged between each half of the cortex to give a single measurement for each embryo.

Image analysis – Intensity Profile Extraction: To plot CDC-42 profiles a 60 x 60 area was selected cutting across a stripe of straightened cortex at the anterior most of each zygote. The intensity values in this area were averaged in the Y- axis leading to an intensity profile encompassing the cell membrane. The cytoplasmic level of each profile was set to one by dividing the profile values by the average of a cytoplasmic section (last 16 pixels). For representation, all normalised intensity profiles were centred around their highest values, corresponding to the membrane/cortex. This analysis was performed on images of maintenance stage embryos – defined as pronuclear meet to metaphase.

Image analysis – Diffusion coefficient and track length: TIRF imaging data was analysed using bespoke MATLAB software[109] to track and quantify the intensity of particles as a function of time. Briefly, centroids were determined using iterative Gaussian masking and intensity calculated using the summed intensity inside a circular region of interest (3 pixel radius), and corrected for the local background in a 10 pixel wide square region of interest around the particle. Particles were linked together in trajectories based on a linking distance of 4 pixels and accepted if their signal to noise ratio was above 0.4 and lasted longer than 3 frames. Diffusion coefficients were calculated by a linear fit to the first 4 mean-squared displacements as a function of time interval (τ).[110] Probability distributions of diffusion coefficients were made from normalised histograms and fit using multiple Gamma functions.[111] Here, a two Gamma function model comprising a mobile and immobile population to yield the diffusion coefficient of the mobile population and proportion of tracks in the immobile population was used:

$$G(x) = A_1\left(\frac{n}{D_1}\right)^n x^{n-1} exp\left(-\frac{nx}{D_1(n-1)!}\right) + (1-A_1)\left(\frac{n}{D_2}\right)^n x^{n-1} exp\left(-\frac{nx}{D_2(n-1)!}\right)$$

Where G(x) is the probability of a track having x diffusion coefficient; n is the number of mean squared displacement values used in the diffusion coefficient fits, A_1 is the proportion of immobile particles and D_1 and D_2 are the population immobile and mobile diffusion coefficients respectively.

SMAUG algorithm was run on the raw linked trajectory position data from CDC-42 wild-type variant to identify the number of mobility states. Iterations were started with 10 mobility states, 15ms frame time and 100nm pixel size, the rest of parameters were kept as default.[79]

Simulated data was generated by simulating image stacks of Gaussian approximated point spread functions with the same intensity (75 kcounts), background (17 kcounts) and noise (250 counts standard deviation) as found in real TIRF images of GFP::CDC42 in live embryos. Brownian motion with diffusion coefficient of 0.65$\mu m^2/s$ in trajectories was simulated and image stacks tracked with the same Matlab algorithm as for real image data.

sc-SiMPull data anaylsis: The raw TIRF movies from sc-SiMPull experiments were processed using open-source software written in MATLAB and available at https://github.com/Dickinson-lab/SiMPull-Analysis-Software.[26] The software uses a sliding window subtraction approach followed by image segmentation to identify single bait protein capture events. Each bait protein capture event is checked for presence of a corresponding prey protein signal; simultaneous binding of bait and prey proteins to the coverslip (termed co-appearance) indicates that the proteins are in complex. After identifying GFP::CDC-42 / HaloTag::aPKC complexes in this way, the dwell time of the HaloTag signal (i.e., the time from its appearance to its disappearance) was measured. The distribution of dwell times was converted to a disappearance rate constant $k_{disappear}$ using a Bayesian inference approach that yields both the maximum likelihood value for $k_{disappear}$ and its 95% credible interval.[112] $k_{disappear}$ is the sum of the dissociation rate constant k_{off} and the photobleaching rate constant k_{bleach}. To correct for photobleaching and extract the value of k_{off}, we measured k_{bleach} using a YFP::HaloTag fusion protein (for which $k_{off} = 0$).[26] Each measurement of $k_{disappear}$ was converted to a k_{off} using a splitting probability analysis[80] and single-embryo measurements of k_{off} are plotted as grey circles in **Fig. 2F**. Briefly, we used the value of k_{bleach} from a matched control experiment to calculate the number of molecular disappearance events that are expected due to photobleaching in each dataset. Disappearance events in excess of this expected value are inferred to be due to dissociation, and the frequency of these events is used to infer k_{off} and its 95% credible interval. The splitting probability approach is equivalent to calculating k_{off} by simple subtraction ($k_{off} = k_{disappear} - k_{bleach}$), but is more rigorous because it allows us to account for error in the estimate of k_{bleach} (See Deutz et al.[80] for details).

Image analysis – Differences in PKC-3 vs PAR-3 domain size: Analysis performed on midplane images of maintenance stage embryos – defined as pronuclear meet to metaphase. We used custom-built FIJI macro to create cortical flat-outs. Par retraction difference was determined by subtracting the length of PAR-3 domain from the total domain length of PKC-3 for each zygote. The difference in domain sizes (PKC-3 – PAR-3) is plotted in µm.

Image analysis – PKC-3 and PAR-3 anterior co-localisation: Analysis performed on cortical images of maintenance stage embryos – defined as pronuclear meet to metaphase. We used a custom-built FIJI macro to select an 11 µm x 11 µm area of anterior cortex free from debris. The pre-built FIJI plugin ComDet (v.0.0.5) (https://github.com/UU-cellbiology/ComDet) was used to detect particles above set thresholds (size – 4 pixels, intensity – 11) across all images to yield a readout of the levels of colocalisation between particles of PKC-3 and PAR-3.

Image analysis – PKC-3 cortical Asymmetric Index (ASI): Analysis performed on cortical images of maintenance stage embryos – defined as pronuclear meet to metaphase. We used a custom-built FIJI macro to select three 5.5 µm x 5.5 µm areas in the image; one, the background outside the embryo, two, an area of anterior cortex, and three, an area of posterior cortex. Background subtraction was performed on the anterior and posterior areas. Mean pixel intensity for anterior (A) and posterior (P) areas were calculated and imputed into the ASI formula:

$$ASI = \frac{(A - P)}{2(A + P)}$$

All ASI values were normalised to the mean ASI of wild-type embryos. Asymmetry is therefore defined as >=1 and total symmetry as 0.

Image analysis – PKC-3 anterior cortical coefficient of variation (CV): Analysis performed on cortical images of maintenance stage embryos – defined as pronuclear meet to metaphase. Using the same background subtracted anterior selected areas as the ASI analysis, coefficient of variation was calculated as standard deviation divided by the mean pixel intensities;

$$CV = \frac{\sigma}{\mu}$$

Image analysis – NMY-2 coefficient of variation: Coefficient or variation was calculated (as above) on a 33µm x 11µm cortical area that was centred within the embryo to analyse a region where NMY-2 foci are present. The average coefficient of variation of the first 100 frames (100s) of establishment (starting at pronuclei touch) was presented as NMY-2 coefficient of variation for the embryo.

Image analysis – Determining the presence of CDC-42 pS71 and NMY-2 foci: The analyses of CDC-42 pS71 or NMY-2 foci presence was determined by 2D intensity correlation matrix of a squared area encompassing the anterior of each zygote (MATLAB script), followed by the identification of the first local minima by scanning the resultant matrix from the centre with and increasing circumference.[55] The position of this local minima is used as a proxy of foci size and zygotes with average foci size >1.14um were considered as positive. 2D intensity correlation results were compared to blindly sorting embryos with and without foci, confirming our approach.

Image analysis – NMY-2 foci per frame: NMY-2 tracking analysis (using MATLAB) was implemented on the first 100 frames (100s) of establishment following pronuclear touch. All images were aligned to the anterior-posterior axis of the zygote. Firstly, a mask was manually drawn to select the area occupied by the embryo using FIJI. Using a custom MATLAB script, NMY-2 foci in establishment stage embryos were tracked within this masked region using the Kilfoil interpretation of the Crocker-Grier method[113,114] (frame-worked inside our custom-built MATLAB scripts). Foci presenting the following conditions were tracked: 15 pixel diameter and an integrated intensity, defined by Kilfoil, of 7000 and above. Tracks were discarded if they lasted less than 5 seconds and frame skipping was permitted at a two-frame gap. A full list of parameters can be provided upon request.

Image analysis – NMY-2 flow measurements: Actomyosin cortical flow velocity was determined by performing Particle Image velocimetry (PIV) on the time-lapse movies using the freely available PIVlab MATLAB algorithm (pivlab.blogspot.de). A 2-step multi pass with linear window deformation and a final interrogation area of 32 pixels with a step size of 16 pixels were used as settings in the PIVlab code. The resulting 2D velocity fields obtained from PIVlab were then divided into 18 bins along the anteroposterior axis of the embryo with a stripe height of 60 pixels. To determine the posterior velocity, the x-component of the velocity in the posterior across bins 13 to 17 was then spatially averaged in each frame, before performing a temporal average from the start of flow until the start of pseudocleavage. This spatiotemporal average was then compared across the different conditions (**Fig. 5 D**, **E**).

Image analysis – Maintenance NMY-2 cortical intensity measurements: Analysis was performed on images of maintenance phase embryos – defined in the time between NMY-2 puncta disappearance and before nuclear envelope breakdown. An 11µm x 11µm area was selected outside the embryo (background) and in the centre of the anterior and posterior cortex. The mean value pixel intensity of the background was subtracted from both the mean values of anterior and posterior regions to give background subtracted values. The value of the anterior was then divided by that of the posterior to give the plotted ratios.

Embryo lethality – Embryo lethality percentage was calculated by estimating the number of eggs hatched at 15 °C from a 62 to 72-hour time-window (from L4 stage) from a progeny of 3 adult worms and following the formula: 100x larvae/(eggs+larvae). Two independent experiments in duplicate were performed.

Statistical analysis:
For most analysis, significance was assessed using an unpaired, two-tail Student's T test unless otherwise noted, with the following criteria: *p<0.05, **p<0.01, ***p<0.001, ****p<0.0001. Chi-square test was used to determine differences in the number of zygotes with pS71 or NMY-2 foci, with the following criteria: *p<0.05, **p<0.01, ***p<0.001.
For sc-SiMPull data, a single maximum likelihood and credible interval for k_{off} in each genetic background was calculated by pooling the data from all experiments and is shown by coloured bars in **Fig. 2F**. To determine the upper and lower bounds of the confidence interval, the calculation was repeated using the lower and upper bounds (respectively) of the credible interval for k_{bleach}, thereby ensuring that errors in the determination of k_{bleach} are reflected in the credible interval for k_{off}. k_{off} estimates from sc-SiMPull data are considered significantly different from one another if their 95% credible intervals do not overlap.
For HILO data, D is extracted from gamma fitting and error measured from 95% confidence intervals to the fit. D estimates are considered significantly different from one another if their 95% credible intervals do not overlap.
All other data are presented as mean values together with all data points, mean values with indicated (n), mean ± 95% confidence interval (CI) and all data points, mean ± standard error of the mean (SEM) and all data points, mean ± standard deviation (SD) and all data points, or box plots showing all data points and the median and interquartile range (IQR) with whiskers extending to the max and min values.

Acknowledgements

We thank Nathan Goehring (The Francis Crick Institute) and Jonathan Higgins (Newcastle University) for helpful discussions and comments on the manuscript. We also thank Luke Lavis for JaneliaFluor dyes; Eva Zeiser and Julie Ahringer for guidance on the generation of the MosSCI lines; and Artur Ribeiro Fernandes and Daniel St Johnston for help on the generation of MBP recombinant proteins. This work was supported by BBSRC Research Grant BB/R019436/1 (JR, JP), BBSRC PhD studentships (IS, AB), a PhD studentship from Newcastle University (AG), an Undergraduate Research Fellowship from UT Austin (LND), and NIH R01 GM138443 (DJD) and NSF MCB 2237451 (DJD). DJD is a CPRIT scholar supported by the Cancer Prevention and Research Institute of Texas (RR170054). SRN acknowledges funding support from the Department of Atomic Energy (DAE), Govt. of India (Project Identification no. RTI4003, DAE OM no. 1303/2/2019/R&D-II/DAE/2079 dated 11.02.2020). Academy of Medical Sciences Springboard Award (SBF007\100046) (AW). SN acknowledges Cancer Research UK (CC2119, CC2068), the UK Medical Research Council (CC2119, CC2068), and the Wellcome Trust (CC2119, CC2068). We also would like to acknowledge The Newcastle University Bioimaging Facility.

Author Contributions

JR conceived the project, supervised the work and secured funding. JP, AG, AB, IS performed the experiments and analysed the data. LND performed the sc-SiMPull experiments, and LND and DJD analysed the sc-SiMPull data. AW supervised JP in the acquisition and analyses of TIRF data. SRN provided MATLAB scripts and supported NMY-2 video analyses. SE purified the aPKC iota - Par-6 complex. JR wrote the manuscript, all authors discussed and contributed to the final version.

Declaration of interest

The authors declare no competing interest

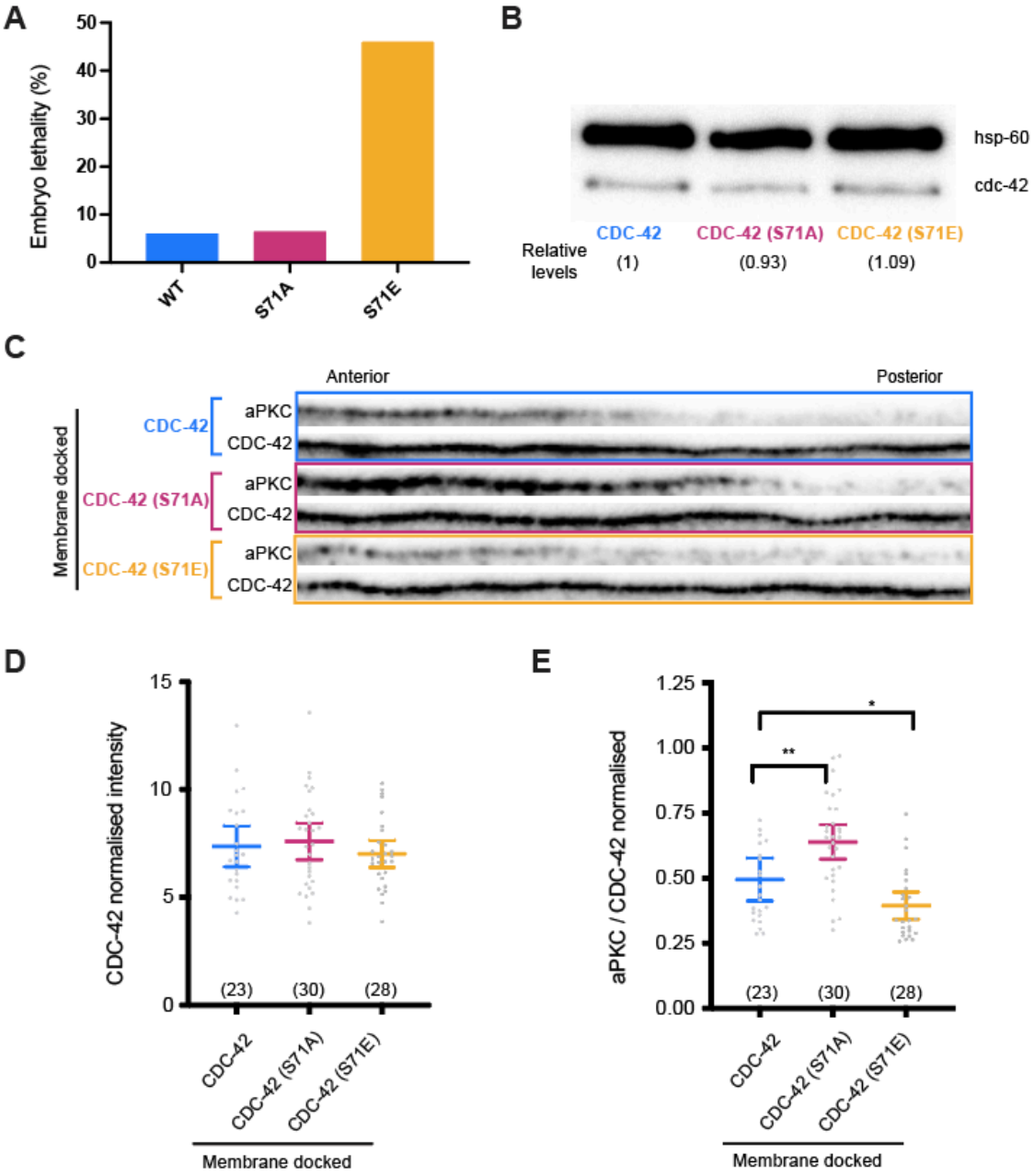

Figure S1. Characterisation of CDC-42 phosphomutant strains. A. Mean embryonic lethality observed for GFP::CDC-42, GFP::CDC-42(S71A) and GFP::CDC-42(S71E) strains in two independent experiment performed in duplicate. Note that in all strains endogenous CDC-42 has been depleted by RNAi of its 3' UTR. **B.** Embryo extract immunoblots showing the protein levels for GFP::CDC-42, GFP::CDC-42(S71A) and GFP::CDC-42(S71E) constructs detected with anti-GFP. Hsp-60 was used as a loading control. Average intensity of CDC-42 in the different strains (loading-corrected) shown relative to the CDC-42 intensity levels in the GFP::CDC-42 wild-type strain (mean from three blots). **C.** Representative flattened-out membranes at the transition from the anterior to the posterior domain. Profiles are centred on 50% of the zygote length and 100 pixels shown in either direction. aPKC (immunofluorescent) and CDC-42 (GFP detection) are shown for the indicated strains during polarity maintenance. Note how GFP::CDC-42, GFP::CDC-42(S71A) and GFP::CDC-42(S71E) are observed throughout the membrane whereas aPKC is still enriched to the anterior side of the zygote. **D.** Measurement of CDC-42 levels in the anterior membrane (measured in a 60 x 60 pixel area from a straightened anterior cortex) of polarity maintenance zygotes. Anterior membrane intensity is normalised with the corresponding CDC-42 cytoplasmic level (mean ± CI 95%). No significant differences are observed between the different strains. **E.** Measurement of aPKC intensity at the anterior membrane normalised to the observed CDC-42 intensity (mean ± CI 95%). After CDC-42 normalisation there is still a significant difference in the levels of anterior aPKC observed for GFP::CDC-42(S71A) and GFP::CDC-42(S71E) when compared to GFP::CDC-42 wild type. In C-E all strains are depleted of the endogenous CDC-42, hence aPKC recruitment is dependent on the ectopically expressed CDC-42 constructs. Total number of embryos analysed indicated in graphs. Unpaired, two-tail Student's t-test *p<0.05.

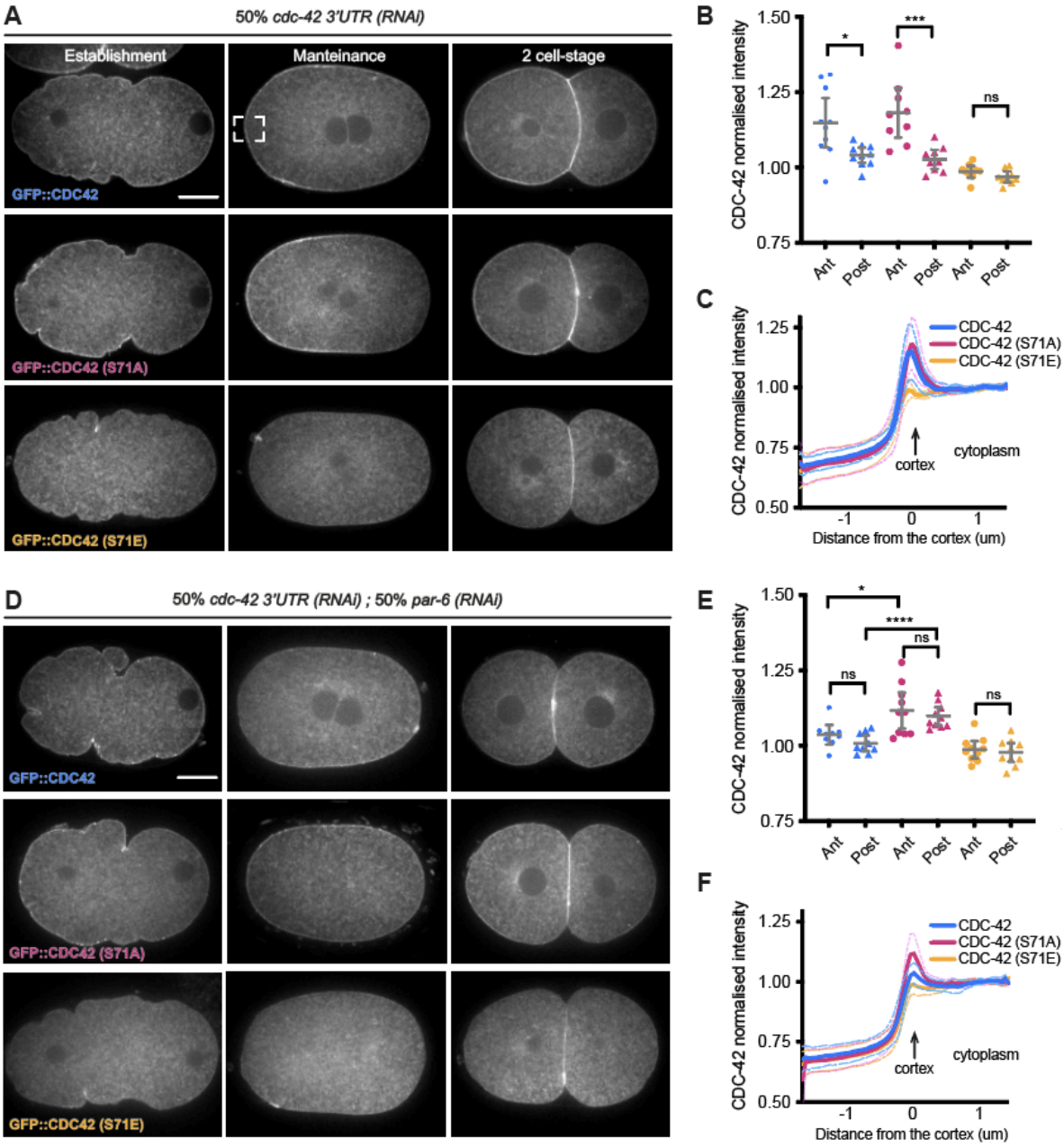

Figure S2. PAR-6 is required for CDC-42 asymmetry and membrane stabilisation. A. Representative midsection confocal images of live embryos at establishment, maintenance and 2-cell stage showing GFP::CDC-42, GFP::CDC-42(S71A) and GFP::CDC-42(S71E). In these CDC-42 reporter lines we depleted endogenous CDC-42 by 50% RNAi of its 3' UTR. Note that the phenotypes observed in this RNAi conditions are very similar to those observed when we deplete CDC-42 by 100% RNAi of its 3'UTR (Fig. 1D-F) **B.** CDC-42 anterior and posterior cortical intensities (values are normalised by their corresponding cytoplasmic CDC-42 levels) observed in CDC-42, CDC-42(S71A) and CDC-42(S71E) maintenance stage embryos (mean ± CI 95%). **C.** CDC-42 intensity profiles spanning the anterior membrane of CDC-42, CDC-42(S71A) and CDC-42(S71E) maintenance stage zygotes, showing mean ± SD. Briefly a 60 x 60 pixel area from a straightened anterior cortex (see inset in A in GFP::CDC-42 maintenance) was projected in the y-axis to give a cross section profile spanning the cortex/membrane. The values are normalised so that the cytoplasmic levels are set to 1. Number of embryos studied in B. and C.: 10 CDC-42, 9 CDC-42(S71A), and 9 CDC-42(S71E) **D. E. F.** show the zygotes and analyses of the GFP::CDC-42, GFP::CDC-42(S71A) and GFP::CDC-42(S71E) strains upon 50% RNAi depletion of both, PAR-6 and endogenous CDC-42. Note that in this condition GFP::CDC-42 and GFP::CDC-42(S71A) lose their asymmetric localisation (E) just like GFP::CDC-42(S71E) upon depletion of only endogenous CDC-42 (B). However, GFP::CDC-42(S71A) retains some of its membrane localisation upon depletion of PAR-6 unlike GFP::CDC-42 (E,F). Number of embryos studied in E. and F.: 9 CDC-42, 10 CDC-42(S71A), and 10 CDC-42(S71E). Unpaired, two-tail Student's t-test *$p<0.05$, ***$p<0.001$, ****$p<0.0001$, ns not significant. Scale bar in establishment zygotes: 10 µm.

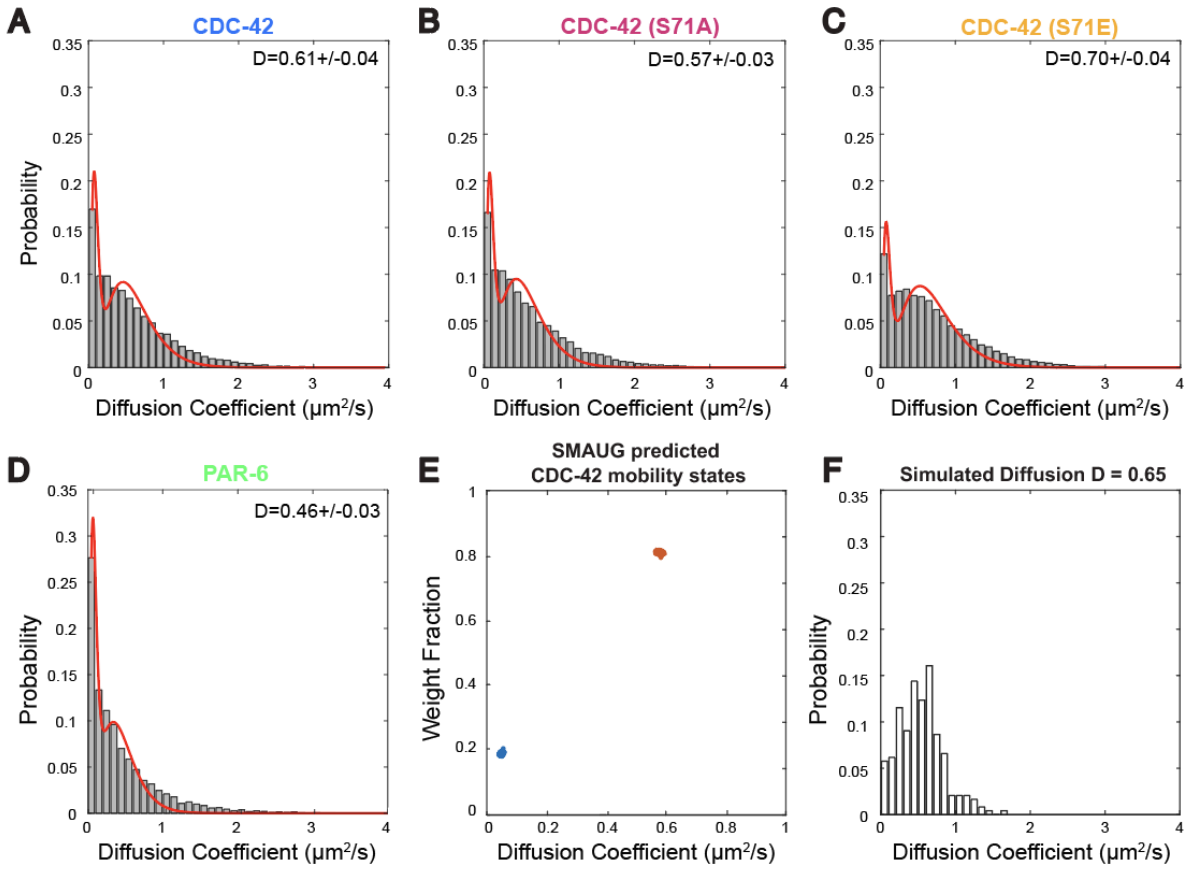

Figure S3. Phosphorylation of CDC-42 accelerates its movement within the membrane. Distribution of diffusion coefficients for CDC-42, CDC-42(S71A), CDC-42(S71E), PAR-6 and simulated data. **A.** to **D.** Double Gamma fits (red curve) to each distribution captures two mobility states for each CDC-42 variant and for PAR-6, mobile (D> 0.1 $\mu m^2/s$) and immobile (D< 0.1 $\mu m^2/s$). Diffusion coefficient of the mobile fraction indicated above each graph (data also shown in Fig. 1H). **E.** We further confirmed two states in our CDC-42 diffusion data using nonparametric Bayesian statistics with SMAUG algorithm, which suggested ~20% CDC-42 particles were in an immobile state (blue cluster, D~0.05$\mu m^2/s$), with the remaining mobile population diffusing with D~0.6$\mu m^2/s$ (red cluster), agreeing well with our fitting. **F.** Simulation is done based on real data from the mobile fraction of CDC-42 considering particles moving at 0.65$\mu m^2/s$ (see methods for more details). From the simulation we extract the baseline fraction of apparently immobile particles (0.06) obtained due to inherent errors in fitting mean squared displacement data. We show this baseline in Fig. 1I.

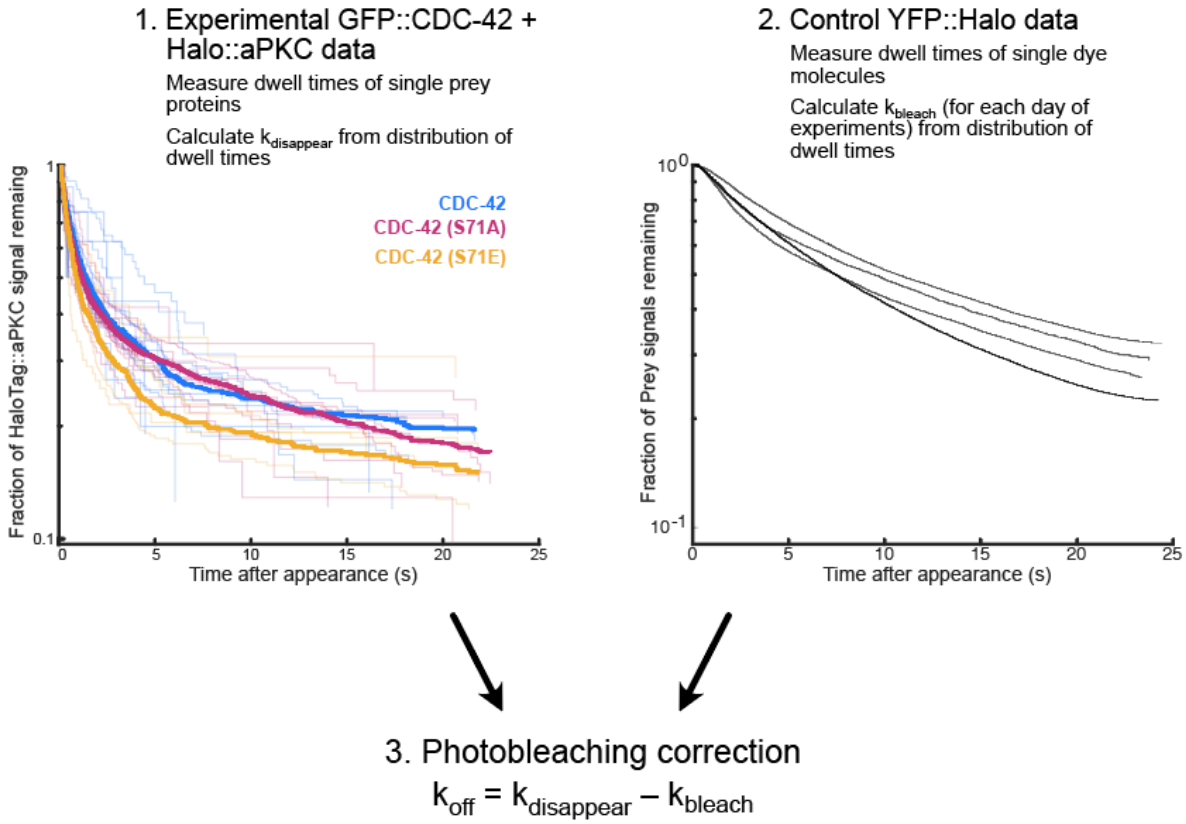

Figure S4. Calculation of k_{off} for the CDC-42/aPKC interaction from Halo:: aPKC signal disappearance. For each identified GFP::CDC-42/Halo::aPKC complex, we measure the survival time (i.e., the dwell time) of the Halo::aPKC prey protein signal (see Fig. 2E for an illustration of the approach). Each dwell time is the interval between GFP::CDC-42/Halo::aPKC complex capture and Halo::aPKC signal disappearance. The distribution of dwell times for the population is represented as a Kaplan-Meier survival curve (step 1), which illustrates the probability of the Halo::aPKC signal remaining present as a function of time since capture. In the plot, thin curves represent single-embryo experiments, and the bold curve represents the sum of all data (obtained by pooling all single-molecule observations regardless of which embryo they originated from). We use the distribution of dwell times to calculate the apparent rate constant $k_{disappear}$ for each single-embryo experiment. Since each Halo::aPKC molecule can disappear due to either unbinding or photobleaching, we separately measured the photobleaching rate of the JF_{646} HaloTag ligand using a YFP::Halo transgenic control strain (step 2). The photobleaching rate constant k_{bleach} is calculated from these data. There is some variability in the photobleaching rate over time, due to fluctuations in laser power and/or microscope alignment, and so each experimental measurement is corrected separately for photobleaching using a paired control measurement captured the same week (step 3). The corrected photobleaching rates are pooled across multiple embryos to obtain a maximum probability estimate of k_{off}, and its 95% credible interval, for each experimental condition. See Deutz et al. 2023 and Methods for details of this calculation.

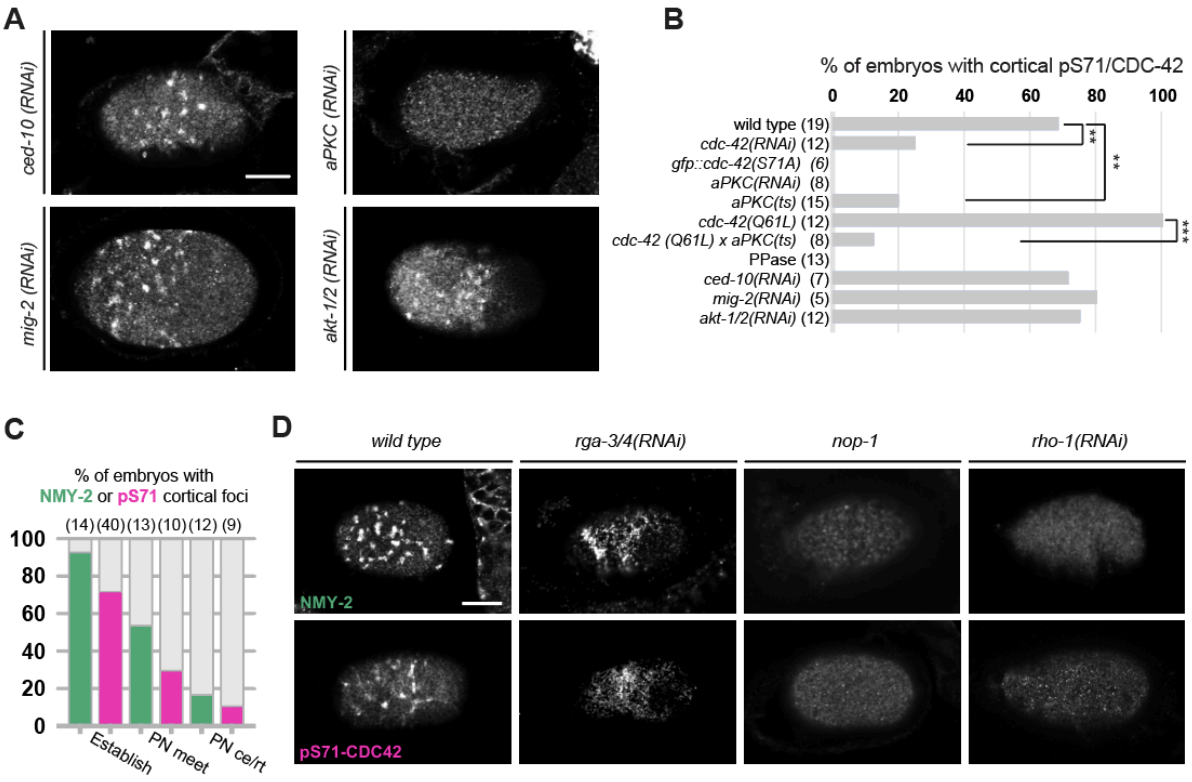

Figure S5. CDC-42 pS71 cortical foci do not depend on Rac1 small GTPases or Akt1 kinase but do depend on the actomyosin organisation. A. Immunofluorescent detection of CDC-42 phosphorylation on serine 71 in polarity establishment zygotes, showing the presence or absence of cortical foci upon depletion of Rac1 homologues (CED-10 and MIG-1) and depletion of aPKC or AKT-1 and AKT-2 kinases (*akt-1/2(RNAi)*). **B.** Quantification showing the percentage of zygotes with CDC-42 pS71 cortical foci inferred from 2D intensity correlation analysis (see methods). For ease of comparison the graph contains data presented in main Fig. 4. **C.** Quantification of zygotes with NMY-2 or CDC-42 pS71 foci during polarity establishment and at the later polarity maintenance stages of pronuclei meet and pronuclei centration/rotation. The number of zygotes with NMY-2 and pS71 foci drops similarly over-time. **D.** Representative cortical confocal images of wild-type, *nop-1* or *rga-3* and *rga-4* RNAi (*rga-3/4*) or *rho-1(RNAi)* depleted embryos at polarity establishment, stained for NMY-2 or CDC-42 pS71. We observed that hyper activation of the RHO-1 pathway, via simultaneous downregulation of the GAPs, RGA-3 and RGA-4, leads to expanded and disorganised CDC-42 pS71 foci similar to those reported for NMY-2 (Michaux et al., 2018; Schmutz et al., 2007; Schonegg et al., 2007; Tse et al., 2012), and in *nop-1* mutant or *rho-1* partial depletion (10% RNAi) where NMY-2 foci are not observed during polarity establishment (Fievet et al., 2013; Tse et al., 2012), we also did not detect CDC-42 pS71 foci. Chi-square test **p<0.01, ***p<0.001. Scale bar: 10 µm.

Bibliography

1. Campanale, J.P., Sun, T.Y., and Montell, D.J. (2017). Development and dynamics of cell polarity at a glance. J Cell Sci *130*, 1201–1207. 10.1242/jcs.188599.
2. Goldstein, B., and Macara, I.G. (2007). The PAR Proteins: Fundamental Players in Animal Cell Polarization. Dev Cell *13*, 609–622. 10.1016/j.devcel.2007.10.007.
3. St Johnston, D., and Ahringer, J. (2010). Cell polarity in eggs and epithelia: Parallels and diversity. Cell *141*, 757–774. 10.1016/j.cell.2010.05.011.
4. Kemphues, K.J., Priess, J.R., Morton, D.G., and Cheng, N.S. (1988). Identification of genes required for cytoplasmic localization in early C. elegans embryos. Cell *52*, 311–320.
5. Watts, J.L., Etemad-Moghadam, B., Guo, S., Boyd, L., Draper, B.W., Mello, C.C., Priess, J.R., and Kemphues, K.J. (1996). par-6, a gene involved in the establishment of asymmetry in early C. elegans embryos, mediates the asymmetric localization of PAR-3. Development *122*, 3133–3140.
6. Tabuse, Y., Izumi, Y., Piano, F., Kemphues, K.J., Miwa, J., and Ohno, S. (1998). Atypical protein kinase C cooperates with PAR-3 to establish embryonic polarity in Caenorhabditis elegans. Development *125*, 3607–3614.
7. Rodriguez-Boulan, E., and Macara, I.G. (2014). Organization and execution of the epithelial polarity programme. Nat Rev Mol Cell Biol *15*, 225–242. 10.1038/nrm3775.
8. Riga, A., Castiglioni, V.G., and Boxem, M. (2020). New insights into apical-basal polarization in epithelia. Curr Opin Cell Biol *62*, 1–8. 10.1016/j.ceb.2019.07.017.
9. Mayor, R., and Etienne-Manneville, S. (2016). The front and rear of collective cell migration. Nat Rev Mol Cell Biol *17*, 97–109. 10.1038/nrm.2015.14.
10. Petrie, R.J., Doyle, A.D., and Yamada, K.M. (2009). Random versus directionally persistent cell migration. Nat Rev Mol Cell Biol *10*, 538–549. 10.1038/nrm2729.
11. Homem, C.C.F., and Knoblich, J.A. (2012). Drosophila neuroblasts: A model for stem cell biology. Development (Cambridge) *139*, 4297–4310. 10.1242/dev.080515.
12. Gallaud, E., Pham, T., and Cabernard, C. (2017). Drosophila melanogaster Neuroblasts: A Model for Asymmetric Stem Cell Divisions. In, pp. 183–210. 10.1007/978-3-319-53150-2_8.
13. Hong, Y. (2018). aPKC: the Kinase that Phosphorylates Cell Polarity. F1000Res *7*, 903. 10.12688/f1000research.14427.1.
14. Atwood, S.X., Chabu, C., Penkert, R.R., Doe, C.Q., and Prehoda, K.E. (2007). Cdc42 acts downstream of Bazooka to regulate neuroblast polarity through Par-6–aPKC. J Cell Sci *120*, 3200–3206. 10.1242/jcs.014902.
15. Graybill, C., Wee, B., Atwood, S.X., and Prehoda, K.E. (2012). Partitioning-defective protein 6 (Par-6) activates atypical protein kinase C (aPKC) by pseudosubstrate displacement. J Biol Chem *287*, 21003–21011.
16. Joberty, G., Petersen, C., Gao, L., and Macara, I.G. (2000). The cell-polarity protein Par6 links Par3 and atypical protein kinase C to Cdc42. Nat Cell Biol *2*.
17. Li, J., Kim, H., Aceto, D.G., Hung, J., Aono, S., and Kemphues, K.J. (2010). Binding to PKC-3, but not to PAR-3 or to a conventional PDZ domain ligand, is required for PAR-6 function in C. elegans. Dev Biol *340*, 88–98.
18. Lin, D., Edwards, A.S., Fawcett, J.P., Mbamalu, G., Scott, J.D., and Pawson, T. (2000). A mammalian PAR-3-PAR-6 complex implicated in Cdc42/Rac1 and aPKC signalling and cell polarity. Nat Cell Biol *2*, 540–547.

19. Qiu, R.G., Abo, A., and Steven Martin, G. (2000). A human homolog of the C. elegans polarity determinant Par-6 links Rac and Cdc42 to PKCzeta signaling and cell transformation. Curr Biol *10*, 697–707.
20. Renschler, F.A., Bruekner, S.R., Salomon, P.L., Mukherjee, A., Kullmann, L., Schütz-Stoffregen, M.C., Henzler, C., Pawson, T., Krahn, M.P., and Wiesner, S. (2018). Structural basis for the interaction between the cell polarity proteins Par3 and Par6. Sci Signal *11*. 10.1126/scisignal.aam9899.
21. Vargas, E., and Prehoda, K.E. (2023). Negative cooperativity underlies dynamic assembly of the Par complex regulators Cdc42 and Par-3. Journal of Biological Chemistry *299*, 102749. 10.1016/j.jbc.2022.102749.
22. Beers, M., and Kemphues, K. (2006). Depletion of the co-chaperone CDC-37 reveals two modes of PAR-6 cortical association in C. elegans embryos. Development *133*, 3745–3754.
23. Johnson, J.L., Erickson, J.W., and Cerione, R.A. (2012). C-terminal Di-arginine motif of Cdc42 protein is essential for binding to phosphatidylinositol 4,5-bisphosphate-containing membranes and inducing cellular transformation. Journal of Biological Chemistry *287*, 5764–5774. 10.1074/jbc.M111.336487.
24. Krahn, M.P., Klopfenstein, D.R., Fischer, N., and Wodarz, A. (2010). Membrane targeting of Bazooka/PAR-3 is mediated by direct binding to phosphoinositide lipids. Curr Biol *20*, 636–642.
25. Roberts, P.J., Mitin, N., Keller, P.J., Chenette, E.J., Madigan, J.P., Currin, R.O., Cox, A.D., Wilson, O., Kirschmeier, P., and Der, C.J. (2008). Rho family GTPase modification and dependence on CAAX motif-signaled posttranslational modification. Journal of Biological Chemistry *283*, 25150–25163. 10.1074/jbc.M800882200.
26. Sarıkaya, S., and Dickinson, D.J. (2021). Rapid extraction and kinetic analysis of protein complexes from single cells. Biophys J *120*, 5018–5031. 10.1016/j.bpj.2021.10.011.
27. Holly, R.W., Jones, K., and Prehoda, K.E. (2020). A Conserved PDZ-Binding Motif in aPKC Interacts with Par-3 and Mediates Cortical Polarity. Current Biology *30*, 893-898.e5. 10.1016/j.cub.2019.12.055.
28. Penkert, R.R., Vargas, E., and Prehoda, K.E. (2022). Energetic determinants of animal cell polarity regulator Par-3 interaction with the Par complex. Journal of Biological Chemistry *298*, 102223. 10.1016/j.jbc.2022.102223.
29. Dong, W., Lu, J., Zhang, X., Wu, Y., Lettieri, K., Hammond, G.R., and Hong, Y. (2020). A polybasic domain in aPKC mediates Par6-dependent control of membrane targeting and kinase activity. *219*.
30. Jones, K.A., Drummond, M.L., and Prehoda, K.E. (2022). Cooperative regulation of C1-domain membrane recruitment polarizes atypical Protein Kinase C.
31. Achilleos, A., Wehman, A.M., and Nance, J. (2010). PAR-3 mediates the initial clustering and apical localization of junction and polarity proteins during C. elegans intestinal epithelial cell polarization. Development *137*, 1833–1842.
32. David, D.J.V., Wang, Q., Feng, J.J., and Harris, T.J.C. (2013). Bazooka inhibits aPKC to limit antagonism of actomyosin networks during amnioserosa apical constriction. Development (Cambridge) *140*, 4719–4729. 10.1242/dev.098491.
33. McCaffrey, L.M., and Macara, I.G. (2009). The Par3/aPKC interaction is essential for end bud remodeling and progenitor differentiation during mammary gland morphogenesis. Genes Dev *23*, 1450–1460.

34. Wirtz-Peitz, F., Nishimura, T., and Knoblich, J.A. (2008). Linking Cell Cycle to Asymmetric Division: Aurora-A Phosphorylates the Par Complex to Regulate Numb Localization. Cell *135*, 161–173.
35. Soriano, E. V, Ivanova, M.E., Fletcher, G., Riou, P., Knowles, P.P., Barnouin, K., Purkiss, A., Kostelecky, B., Saiu, P., Linch, M., et al. (2016). aPKC Inhibition by Par3 CR3 Flanking Regions Controls Substrate Access and Underpins Apical-Junctional Polarization. Dev Cell *38*, 384–398.
36. Rodriguez, J., Peglion, F., Martin, J., Hubatsch, L., Reich, J., Hirani, N., Gubieda, A.G., Roffey, J., Fernandes, A.R., St Johnston, D., et al. (2017). aPKC Cycles between Functionally Distinct PAR Protein Assemblies to Drive Cell Polarity. Dev Cell *42*, 400-415.e9. 10.1016/j.devcel.2017.07.007.
37. Yamanaka, T., Horikoshi, Y., Suzuki, A., Sugiyama, Y., Kitamura, K., Maniwa, R., Nagai, Y., Yamashita, A., Hirose, T., Ishikawa, H., et al. (2001). PAR-6 regulates aPKC activity in a novel way and mediates cell-cell contact-induces formation of the epithelial junctional complex. Genes to Cells *6*, 721–731. 10.1046/j.1365-2443.2001.00453.x.
38. Holly, R.W., and Prehoda, K.E. (2019). Phosphorylation of Par-3 by Atypical Protein Kinase C and Competition between Its Substrates. Dev Cell *49*, 678–679. 10.1016/j.devcel.2019.05.002.
39. Martin-Belmonte, F., Gassama, A., Datta, A., Yu, W., Rescher, U., Gerke, V., and Mostov, K. (2007). PTEN-mediated apical segregation of phosphoinositides controls epithelial morphogenesis through Cdc42. Cell *128*, 383–397.
40. Dickinson, D.J., Schwager, F., Pintard, L., Gotta, M., and Goldstein, B. (2017). A Single-Cell Biochemistry Approach Reveals PAR Complex Dynamics during Cell Polarization. Dev Cell *42*, 416-434.e11. 10.1016/j.devcel.2017.07.024.
41. Lee, C.Y., Andersen, R.O., Cabernard, C., Manning, L., Tran, K.D., Lanskey, M.J., Bashirullah, A., and Doe, C.Q. (2006). Drosophila Aurora-A kinase inhibits neuroblast self-renewal by regulating aPKC/Numb cortical polarity and spindle orientation. Genes Dev *20*, 3464–3474. 10.1101/gad.1489406.
42. Reich, J.D., Hubatsch, L., Illukkumbura, R., Peglion, F., Bland, T., Hirani, N., and Goehring, N.W. (2019). Regulated Activation of the PAR Polarity Network Ensures a Timely and Specific Response to Spatial Cues. Current Biology *29*, 1911-1923.e5. 10.1016/j.cub.2019.04.058.
43. Benton, R., and St Johnston, D. (2003). Drosophila PAR-1 and 14-3-3 inhibit Bazooka/PAR-3 to establish complementary cortical domains in polarized cells. Cell *115*, 691–704.
44. Chen, Y.M., Wang, Q.J., Hu, H.S., Yu, P.C., Zhu, J., Drewes, G., Piwnica-Worms, H., and Luo, Z.G. (2006). Microtubule affinity-regulating kinase 2 functions downstream of the PAR-3/PAR-6/atypical PKC complex in regulating hippocampal neuronal polarity. Proc Natl Acad Sci U S A *103*, 8534–8539.
45. Hurov, J.B., Watkins, J.L., and Piwnica-Worms, H. (2004). Atypical PKC phosphorylates PAR-1 kinases to regulate localization and activity. Curr Biol *14*, 736–741.
46. Motegi, F., Zonies, S., Hao, Y., Cuenca, A.A., Griffin, E., and Seydoux, G. (2011). Microtubules induce self-organization of polarized PAR domains in Caenorhabditis elegans zygotes. Nat Cell Biol.
47. Suzuki, A., Hirata, M., Kamimura, K., Maniwa, R., Yamanaka, T., Mizuno, K., Kishikawa, M., Hirose, H., Amano, Y., Izumi, N., et al. (2004). aPKC acts upstream of PAR-1b in

both the establishment and maintenance of mammalian epithelial polarity. Curr Biol *14*, 1425–1435.

48. Hannaford, M., Loyer, N., Tonelli, F., Zoltner, M., and Januschke, J. (2019). A chemical-genetics approach to study the role of atypical protein kinase C in Drosophila. Development (Cambridge) *146*. 10.1242/dev.170589.
49. Cheeks, R., Canman, J., Gabriel, W., Meyer, N., Strome, S., and Goldstein, B. (2004). C. elegans PAR Proteins Function by Mobilizing and Stabilizing Asymmetrically Localized Protein Complexes. Current Biology *14*, 851–862.
50. Munro, E., Nance, J., and Priess, J.R. (2004). Cortical flows powered by asymmetrical contraction transport PAR proteins to establish and maintain anterior-posterior polarity in the early C. elegans embryo. Dev Cell. 10.1016/j.devcel.2004.08.001.
51. Motegi, F., and Sugimoto, A. (2006). Sequential functioning of the ECT-2 RhoGEF, RHO-1 and CDC-42 establishes cell polarity in Caenorhabditis elegans embryos. Nat Cell Biol *8*, 978–985. 10.1038/ncb1459.
52. Schonegg, S., and Hyman, A.A. (2006). CDC-42 and RHO-1 coordinate acto-myosin contractility and PAR protein localization during polarity establishment in C. elegans embryos. Development *133*, 3507–3516. 10.1242/dev.02527.
53. Nishikawa, M., Naganathan, S.R., Jülicher, F., and Grill, S.W. (2017). Controlling contractile instabilities in the actomyosin cortex. Elife *6*, 1–21. 10.7554/eLife.19595.
54. Michaux, J.B., Robin, F.B., McFadden, W.M., and Munro, E.M. (2018). Excitable RhoA dynamics drive pulsed contractions in the early C. elegans embryo. J Cell Biol *217*, 4230–4252. 10.1083/jcb.201806161.
55. Naganathan, S.R., Fürthauer, S., Rodriguez, J., Fievet, B.T., Jülicher, F., Ahringer, J., Cannistraci, C.V., and Grill, S.W. (2018). Morphogenetic degeneracies in the actomyosin cortex. Elife *7*, 1–21. 10.7554/eLife.37677.
56. Aceto, D., Beers, M., and Kemphues, K.J. (2006). Interaction of PAR-6 with CDC-42 is required for maintenance but not establishment of PAR asymmetry in C. elegans. Dev Biol *299*, 386–397.
57. Hung, T.J., and Kemphues, K.J. (1999). PAR-6 is a conserved PDZ domain-containing protein that colocalizes with PAR-3 in Caenorhabditis elegans embryos. Development *126*, 127–135.
58. Chang, Y., and Dickinson, D.J. (2022). A particle size threshold governs diffusion and segregation of PAR-3 during cell polarization. Cell Rep *39*, 110652. 10.1016/j.celrep.2022.110652.
59. Goehring, N.W., Trong, P.K., Bois, J.S., Chowdhury, D., Nicola, E.M., Hyman, A.A., and Grill, S.W. (2011). Polarization of PAR proteins by advective triggering of a pattern-forming system. Science (1979) *334*, 1137–1141. 10.1126/science.1208619.
60. Zmurchok, C., and Holmes, W.R. (2021). Biophysical Models of PAR Cluster Transport by Cortical Flow in C . elegans Early Embryogenesis. 1–26.
61. Oon, C.H., and Prehoda, K.E. (2019). Asymmetric recruitment and actin-dependent cortical flows drive the neuroblast polarity cycle. Elife *8*, 1–15. 10.7554/eLife.45815.
62. Wang, S.C., Low, T.Y.F., Nishimura, Y., Gole, L., Yu, W., and Motegi, F. (2017). Cortical forces and CDC-42 control clustering of PAR proteins for Caenorhabditis elegans embryonic polarization. Nat Cell Biol *19*, 988–995. 10.1038/ncb3577.
63. Illukkumbura, R., Hirani, N., Borrego-Pinto, J., Bland, T., Ng, K.B., Hubatsch, L., McQuade, J., Endres, R.G., and Goehring, N.W. (2023). Design principles for selective polarization of PAR proteins by cortical flows. J Cell Biol *222*. 10.1083/jcb.202209111.

64. Boyd, L., Guo, S., Levitan, D., Stinchcomb, D.T., and Kemphues, K.J. (1996). PAR-2 is asymmetrically distributed and promotes association of P granules and PAR-1 with the cortex in C. elegans embryos. Development *122*, 3075–3084.
65. Hao, Y., Boyd, L., and Seydoux, G. (2006). Stabilization of cell polarity by the C. elegans RING protein PAR-2. Dev Cell *10*, 199–208.
66. Hoege, C., Constantinescu, A.-T., Schwager, A., Goehring, N.W., Kumar, P., and Hyman, A.A. (2010). LGL can partition the cortex of one-cell Caenorhabditis elegans embryos into two domains. Curr Biol *20*, 1296–1303.
67. Sailer, A., Anneken, A., Li, Y., Lee, S., and Munro, E. (2015). Dynamic Opposition of Clustered Proteins Stabilizes Cortical Polarity in the C. elegans Zygote. Dev Cell *35*, 131–142.
68. Beatty, A., Morton, D., and Kemphues, K. (2010). The C. elegans homolog of Drosophila lethal giant larvae functions redundantly with PAR-2 to maintain polarity in the early embryo. Development *137*, 3995–4004. 10.1242/dev.056028.
69. Kumfer, K.T., Cook, S.J., Squirrell, J.M., Eliceiri, K.W., Peel, N., O'Connell, K.F., and White, J.G. (2010). CGEF-1 and CHIN-1 Regulate CDC-42 Activity during Asymmetric Division in the Caenorhabditis elegans Embryo. Mol Biol Cell *21*, 266–277. 10.1091/mbc.E09.
70. Wang, C., Xu, H., Lin, S., Deng, W., Zhou, J., Zhang, Y., Shi, Y., Peng, D., and Xue, Y. (2020). GPS 5.0: An Update on the Prediction of Kinase-specific Phosphorylation Sites in Proteins. Genomics Proteomics Bioinformatics *18*, 72–80. 10.1016/j.gpb.2020.01.001.
71. Schoentaube, J., Olling, A., Tatge, H., Just, I., and Gerhard, R. (2009). Serine-71 phosphorylation of Rac1/Cdc42 diminishes the pathogenic effect of Clostridium difficile toxin A. Cell Microbiol *11*, 1816–1826. 10.1111/j.1462-5822.2009.01373.x.
72. Schwarz, J., Proff, J., Hävemeier, A., Ladwein, M., Rottner, K., Barlag, B., Pich, A., Tatge, H., Just, I., and Gerhard, R. (2012). Serine-71 phosphorylation of Rac1 modulates downstream signaling. PLoS One *7*, e44358.
73. Pothula, S., Bazan, H.E.P., and Chandrasekher, G. (2013). Regulation of cdc42 expression and signaling is critical for promoting corneal epithelial wound healing. Invest Ophthalmol Vis Sci *54*, 5343–5352. 10.1167/iovs.13-11955.
74. Gunaratne, A., Thai, B.L., and Di Guglielmo, G.M. (2013). Atypical Protein Kinase C Phosphorylates Par6 and Facilitates Transforming Growth Factor β-Induced Epithelial-to-Mesenchymal Transition. Mol Cell Biol *33*, 874–886. 10.1128/mcb.00837-12.
75. Tokunaga, M., Imamoto, N., and Sakata-Sogawa, K. (2008). Highly inclined thin illumination enables clear single-molecule imaging in cells. Nat Methods *5*, 159–161. 10.1038/NMETH.1171.
76. Gubieda, A.G., Packer, J.R., Squires, I., Martin, J., and Rodriguez, J. (2020). Going with the flow: insights from Caenorhabditis elegans zygote polarization. Philos Trans R Soc Lond B Biol Sci *375*, 20190555. 10.1098/rstb.2019.0555.
77. Illukkumbura, R., Bland, T., and Goehring, N.W. (2020). Patterning and polarization of cells by intracellular flows. Curr Opin Cell Biol *62*, 123–134. 10.1016/j.ceb.2019.10.005.
78. Robin, F.B., Mcfadden, W.M., Yao, B., and Munro, E.M. (2014). Single-molecule analysis of cell surface dynamics in Caenorhabditis elegans embryos. Nat Methods *11*, 677–682.

79. Karslake, J.D., Donarski, E.D., Shelby, S.A., Demey, L.M., DiRita, V.J., Veatch, S.L., and Biteen, J.S. (2021). SMAUG: Analyzing single-molecule tracks with nonparametric Bayesian statistics. Methods *193*, 16–26. 10.1016/j.ymeth.2020.03.008.
80. Deutz, L.N., Sarıkaya, S., and Dickinson, D.J. (2023). Membrane extraction in native lipid nanodiscs reveals dynamic regulation of Cdc42 complexes during cell polarization. 1–35.
81. Etienne-Manneville, S. (2004). Cdc42--the centre of polarity. J Cell Sci *117*, 1291–1300.
82. Sit, S.-T., and Manser, E. (2011). Rho GTPases and their role in organizing the actin cytoskeleton. J Cell Sci *124*, 679–683.
83. Kwon, T., Kwon, D.Y., Chun, J., Kim, J.H., and Kang, S.S. (2000). Akt protein kinase inhibits Rac1-GTP binding through phosphorylation at serine 71 of Rac1. J Biol Chem *275*, 423–428.
84. Fievet, B.T., Rodriguez, J., Naganathan, S., Lee, C., Zeiser, E., Ishidate, T., Shirayama, M., Grill, S., and Ahringer, J. (2013). Systematic genetic interaction screens uncover cell polarity regulators and functional redundancy. Nat Cell Biol *15*, 103–112. 10.1038/ncb2639.
85. Gross, P., Kumar, K.V., Goehring, N.W., Bois, J.S., Hoege, C., Jülicher, F., and Grill, S.W. (2019). Guiding self-organized pattern formation in cell polarity establishment. Nat Phys *15*, 293–300. 10.1038/s41567-018-0358-7.
86. Mayer, M., Depken, M., Bois, J.S., Jülicher, F., and Grill, S.W. (2010). Anisotropies in cortical tension reveal the physical basis of polarizing cortical flows. Nature *467*, 617–621. 10.1038/nature09376.
87. Reymann, A.C., Staniscia, F., Erzberger, A., Salbreux, G., and Grill, S.W. (2016). Cortical flow aligns actin filaments to form a furrow. Elife *5*, 1–25. 10.7554/eLife.17807.
88. Garrard, S.M., Capaldo, C.T., Gao, L., Rosen, M.K., Macara, I.G., and Tomchick, D.R. (2003). Structure of Cdc42 in a complex with the GTPase-binding domain of the cell polarity protein, Par6. EMBO J *22*, 1125–1133.
89. Peterson, F.C., Penkert, R.R., Volkman, B.F., and Prehoda, K.E. (2004). Cdc42 regulates the Par-6 PDZ domain through an allosteric CRIB-PDZ transition. Mol Cell *13*, 665–676.
90. Hakoshima, T., Shimizu, T., and Maesaki, R. (2003). Structural Basis of the Rho GTPase Signaling. J Biochem *134*, 327–331. 10.1093/jb/mvg149.
91. Nagai-Tamai, Y., Mizuno, K., Hirose, T., Suzuki, A., and Ohno, S. (2002). Regulated protein-protein interaction between aPKC and PAR-3 plays an essential role in the polarization of epithelial cells. Genes to Cells *7*, 1161–1171. 10.1046/j.1365-2443.2002.00590.x.
92. Morais-de-Sá, E., Mirouse, V., and St Johnston, D. (2010). aPKC phosphorylation of Bazooka defines the apical/lateral border in Drosophila epithelial cells. Cell *141*, 509–523.
93. Walther, R.F., and Pichaud, F. (2010). Crumbs/DaPKC-dependent apical exclusion of Bazooka promotes photoreceptor polarity remodeling. Curr Biol *20*, 1065–1074.
94. Betschinger, J., Mechtler, K., and Knoblich, J.A. (2003). The Par complex directs asymmetric cell division by phosphorylating the cytoskeletal protein Lgl. Nature *422*, 326–330.
95. Dong, W., Zhang, X., Liu, W., Chen, Y. jiun, Huang, J., Austin, E., Celotto, A.M., Jiang, W.Z., Palladino, M.J., Jiang, Y., et al. (2015). A conserved polybasic domain mediates

plasma membrane targeting of Lgl and its regulation by hypoxia. Journal of Cell Biology *211*, 273–286. 10.1083/jcb.201503067.

96. Bailey, M.J., and Prehoda, K.E. (2015). Establishment of Par-Polarized Cortical Domains via Phosphoregulated Membrane Motifs. Dev Cell *35*, 199–210.
97. Brzeska, H., Guag, J., Remmert, K., Chacko, S., and Korn, E.D. (2010). An experimentally based computer search identifies unstructured membrane-binding sites in proteins: Application to class I myosins, PAKs, and CARMIL. Journal of Biological Chemistry *285*, 5738–5747. 10.1074/jbc.M109.066910.
98. Ziman, M., Preuss, D., Mulholland, J., O'Brien, J.M., Botstein, D., and Johnson, D.I. (1993). Subcellular localization of Cdc42p, a Saccharomyces cerevisiae GTP-binding protein involved in the control of cell polarity. Mol Biol Cell *4*, 1307–1316. 10.1091/mbc.4.12.1307.
99. Wu, W.J., Erickson, J.W., Lin, R., and Cerione, R.A. (2000). The γ-subunit of the coatomer complex binds Cdc42 to mediate transformation. Nature *405*, 800–804. 10.1038/35015585.
100. Hall, A. (1998). Rho GTpases and the actin cytoskeleton. Science (1979) *279*, 509–514. 10.1126/science.279.5350.509.
101. Hannaford, M.R., Ramat, A., Loyer, N., and Januschke, J. (2018). aPKC-mediated displacement and actomyosin-mediated retention polarize Miranda in Drosophila neuroblasts. Elife *7*, 1–22. 10.7554/eLife.29939.
102. Brenner, S. (1974). THE GENETICS OF CAENORHABDITIS ELEGANS. Genetics *77*, 71–94. 10.1093/genetics/77.1.71.
103. Zeiser, E., Frøkjær-Jensen, C., Jorgensen, E., and Ahringer, J. (2011). MosSCI and gateway compatible plasmid toolkit for constitutive and inducible expression of transgenes in the c. elegans germline. PLoS One *6*, 3–8. 10.1371/journal.pone.0020082.
104. Frøkjær-Jensen, C., Davis, M.W., Ailion, M., and Jorgensen, E.M. (2012). Improved Mos1-mediated transgenesis in C. elegans. Nat Methods *9*, 117–118.
105. Kamath, R.S., Fraser, A.G., Dong, Y., Poulin, G., Durbin, R., Gotta, M., Kanapin, A., Le Bot, N., Moreno, S., Sohrmann, M., et al. (2003). Systematic functional analysis of the Caenorhabditis elegans genome using RNAi. Nature *421*, 231–237.
106. Andrews, R., and Ahringer, J. (2007). Asymmetry of early endosome distribution in C. elegans embryos. PLoS One *2*, e493.
107. Grimm, J.B., English, B.P., Chen, J., Slaughter, J.P., Zhang, Z., Revyakin, A., Patel, R., Macklin, J.J., Normanno, D., Singer, R.H., et al. (2015). A general method to improve fluorophores for live-cell and single-molecule microscopy. Nat Methods *12*, 244–250. 10.1038/nmeth.3256.
108. Schindelin, J., Arganda-Carrera, I., Frise, E., Verena, K., Mark, L., Tobias, P., Stephan, P., Curtis, R., Stephan, S., Benjamin, S., et al. (2009). Fiji - an Open platform for biological image analysis. Nat Methods *9*. 10.1038/nmeth.2019.Fiji.
109. Wollman, A.J.M., Shashkova, S., Hedlund, E.G., Friemann, R., Hohmann, S., and Leake, M.C. (2017). Transcription factor clusters regulate genes in eukaryotic cells. Elife *6*, 1–36. 10.7554/eLife.27451.
110. Kusumi, A., Sako, Y., and Yamamoto, M. (1993). Confined Lateral Diffusion of Membrane Receptors. Biophys J *65*, 2021–2040.
111. Syeda, A.H., Wollman, A.J.M., Hargreaves, A.L., Howard, J.A.L., Bruning, J.G., McGlynn, P., and Leake, M.C. (2019). Single-molecule live cell imaging of Rep reveals

the dynamic interplay between an accessory replicative helicase and the replisome. Nucleic Acids Res *47*, 6287–6298. 10.1093/nar/gkz298.

112. Kinz-Thompson, C.D., Bailey, N.A., and Gonzalez, R.L. (2016). Precisely and Accurately Inferring Single-Molecule Rate Constants. Methods Enzymol *581*, 187–225. 10.1016/bs.mie.2016.08.021.
113. Gao, Y., and Kilfoil, M.L. (2009). Accurate detection and complete tracking of large populations of features in three dimensions. Opt Express *17*, 4685. 10.1364/OE.17.004685.
114. Crocker, J., and Grier, D. (1995). Methods of Digital Video Microscopy for Colloidal Studies | Elsevier Enhanced Reader. J Colloid Interface Sci *179*, 298–310.